Chemie der Erde 77 (2017) 547–572

Contents lists available at ScienceDirect

Chemie der Erde

journal homepage: www.elsevier.de/chemer

Invited Review

X-ray computed tomography of planetary materials: A primer and review of recent studies

Romy D. Hanna*, Richard A. Ketcham

Jackson School of Geosciences, University of Texas, 2275 Speedway Stop C9000, Austin, TX 78712, USA

ARTICLE INFO

Article history:
Received 1 June 2016
Received in revised form
22 December 2016
Accepted 12 January 2017
Editorial handling - Klaus Keil

Keywords:
X-ray
Computed tomography
3D imaging
Synchrotron
Radiation
Damage
Planetary
Meteorites

ABSTRACT

X-ray computed tomography (XCT) is a powerful 3D imaging technique that has been used to investigate meteorites, mission-returned samples, and other planetary materials of all scales from dust particles to large rocks. With this technique, a 3D volume representing the X-ray attenuation (which is sensitive to composition and density) of the materials within an object is produced, allowing various components and textures to be observed and quantified. As with any analytical technique, a thorough understanding of the underlying physical principles, system components, and data acquisition parameters provides a strong foundation for the optimal acquisition and interpretation of the data. Here we present a technical overview of the physics of XCT, describe the major components of a typical laboratory-based XCT instrument, and provide a guide for how to optimize data collection for planetary materials using such systems. We also discuss data processing, visualization and analysis, including a discussion of common data artifacts and how to minimize them. We review a variety of recent studies in which XCT has been used to study extraterrestrial materials and/or to address fundamental problems in planetary science. We conclude with a short discussion of anticipated future directions of XCT technology and application.

Contents

---

* Corresponding author.
E-mail address: romy@jsg.utexas.edu (R.D. Hanna).

http://dx.doi.org/10.1016/j.chemer.2017.01.006

1. Introduction

X-ray computed tomography (XCT) has exploded in popularity over the last two decades as a powerful, non-destructive method to characterize objects in three dimensions. Similar to medical CAT scanning in its basic principles and underlying physics, XCT as applied in the physical sciences utilizes higher energies, smaller X-ray focal spot sizes, and/or longer acquisition times (up to a few hours) to enable higher resolution and superior quality data not attainable in medical settings where dose limitation and subject movement are concerns. In recent years, XCT technology has evolved such that smaller systems are approaching the cost of a high-end scanning electron microscope (SEM) and, thus, more academic and research laboratories are acquiring them to complement other analytical techniques.

The application of X-ray CT for non-medical research purposes began in earnest in the early 1980s after the initial development of medical instruments in the 1960s and 1970s (Hounsfield, 1973, 1976). In the planetary sciences, XCT was applied fairly early as an imaging and qualitative investigation tool for meteorites (Arnold et al., 1983; Hirano et al., 1990; Kondo et al., 1997; Masuda et al., 1986). However, limited access to XCT facilities and expertise prevented its wide application, and it was several years before the first studies aimed at addressing particular planetary problems via the 3D quantification capabilities of XCT appeared (e.g., Gnos et al., 2002; Kuebler et al., 1999; Rubin et al., 2001; Tsuchiyama et al., 2000).

As a non-destructive technique, XCT is particularly useful for documenting and analyzing rare and/or irreplaceable specimens such as meteorites or returned samples (e.g., Apollo, Stardust, Hayabusa), where sample preservation is of particular concern (Blumenfeld et al., 2015; Flynn et al., 2000; Masuda et al., 1986; Tsuchiyama et al., 2002; Zeigler et al., 2014). Using XCT, the entirety of a sample can be imaged prior to slabbing, sectioning, or distribution to museums and researchers. This not only allows digital curation of the sample but also preserves the 3D context of any subsamples to the original sample and to each other. In addition, the XCT data can be used to characterize macroscale features such as sample heterogeneity, pore structure, and/or petrofabrics that may not be noticeable or measurable with traditional 2D microanalytical techniques (e.g., Benedix et al., 2008; Friedrich and Rivers, 2013; Hanna et al., 2015; Zolensky et al., 2014).

There are several review papers that cover different aspects of XCT as it applies to various geoscientific problems (Cnudde and Boone, 2013; Ebel and Rivers, 2007; Fusseis et al., 2014; Ketcham and Carlson, 2001; Kyle and Ketcham, 2015; Wildenschild and Sheppard, 2013). A recent review by Fusseis et al. (2014) focuses on the application of synchrotron CT to geology and rock mechanics and compiles information on the major synchrotron beamlines available for research around the world, as well as helpful information on how to apply for beam time at these facilities. Wildenschild and Sheppard (2013) focus on the application of XCT to porosity measurement and include a discussion of current and future XCT hardware technology. A more generalized review of XCT in geosciences using both X-ray tubes as well as synchrotron X-ray sources is given by Cnudde and Boone (2013). Ebel and Rivers (2007) provide an informative review of meteoritical investigations and applications, mainly using synchrotron-based XCT, including details on an XCT beam line (13-BM-D) at the Advanced Photon Source (APS) at Argonne National Laboratory. The present contribution provides an updated overview of XCT investigation of planetary materials with emphasis on more widely used and available lab-based XCT systems.

Our primary goal is to acquaint the general planetary and geochemical science communities with XCT as it applies to extraterrestrial materials, including details on data acquisition and its optimization for different curatorial and research goals. Because of the proliferation of laboratory-based polychromatic cone-beam XCT instruments (in contrast to more specialized systems with synchrotron sources or a helical acquisition geometry), we will focus on the technology, imaging geometry, and data artifacts that are characteristic of these systems, but provide additional details as well as case studies that utilize others. We first give an introduction to the underlying physical principles of XCT, the common components of a laboratory cone-beam system, and how data acquisition parameters are determined and the various trade-offs encountered. We present the numerous ways XCT data can be processed, corrected, visualized, and quantified, with particular emphasis on common data artifacts that are inherent when using polychromatic cone-beam instruments. We then present several recent case studies of how XCT data have been used to address various planetary science problems, and conclude with a short discussion of the future trajectory of XCT. Our intention is that this review serves as a useful primer for planetary scientists to optimize their own XCT data acquisition, be better prepared to interpret and analyze XCT datasets, and be inspired to use this powerful technique to address problems in their own research.

2. Principles and physics of XCT

2.1. X-ray generation

The easiest way to generate X-rays is to bombard a target material (usually a high-atomic-number metal such as tungsten) with high-energy electrons produced by a heated filament, as in a standard X-ray "tube". A continuum of X-ray energies is produced due to various interactions of the incoming free electrons with bound electrons in the target material. The most dominant interaction produces so-called bremsstrahlung radiation, in which incident electrons decelerate due to interactions with target nuclei (bremsstrahlung arises from the German word *bremsen* for brake). The energy of the resulting radiation depends on the amount of electron kinetic energy transferred by this interaction, and so the X-ray radiation emitted features a broad spectrum of energies up to the maximum energy of the incident electrons (i.e., it is polychromatic). The maximum energy is generated when an electron actually collides with the nucleus and all of its kinetic energy is converted to X-ray radiation, although the probability of such a collision is low, which is why the majority of the radiation is emitted at lower energies (Fig. 1) (Hsieh, 2009). The X-ray tube voltage setting represents the electric potential applied across the chamber that will accelerate electrons up to this maximum energy. For example, if the tube voltage is set to 200 kV, the filament electrons will be accelerated fast enough to generate X-rays up to 200 keV, although the mean X-ray energy is much lower than this (Fig. 1). Because the polychromatic nature of this radiation can cause imaging artifacts, a low-attenuation filter can be used to preferentially remove some of these lower energy X-rays (Ketcham and Carlson, 2001). Another source of X-ray radiation is produced when an incident electron ejects an inner-shell electron of a target atom and an outer-shell electron moves inward to fill this hole. Because the outer-shell electron has a higher energy state than the inner-shell electron, its change in energy state gives rise to a characteristic X-ray energy (Fig. 1). The bremsstrahlung and characteristic X-ray radiation actually only represent a small fraction of energy deposited within the target material; the vast majority (>99%) of the incident electron energy is released as heat (Hsieh, 2009). The total X-ray energy output from the target is characterized as the flux (photons/second), although the terms intensity and flux are often used interchangeably (and will be here).

While an X-ray tube system is a relatively cost-effective way to generate X-ray radiation, the limited X-ray flux and polychromatic spectrum can lead to imaging artifacts (Section 4). Synchrotron sources provide a way to overcome these limitations, although their specialized setup and high operational cost limit their availability. A synchrotron uses a large storage ring [typically hundreds of meters in circumference (see Table 3.1 in Willmott, 2011)] to accelerate free electrons generated from an electron gun (i.e., a heated filament similar to that used in an X-ray tube) to even higher velocities. This gives electrons up to several GeV of kinetic energy as they are accelerated to very near the velocity of light. X-ray radiation is generated from the electrons as their trajectory is modified, either by using bending magnets (to maintain a circular arc) or by the use of an insertion device (undulator or wiggler) along a straight-line segment in the ring which forces the electrons to slightly oscillate and emit X-ray radiation. The large amount of radiation produced allows the use of beam filtration that can be 'tuned' to a particular X-ray energy while maintaining a high flux to produce a brilliant (i.e., high flux over a small spatial area with minimal beam divergence) monochromatic beam (Willmott, 2011).

2.2. *X-ray attenuation*

A three-dimensional XCT data set represents the attenuation of X-rays at each point within an object. The general attenuation of X-rays in a material is governed by Lambert-Beer's Law

$$I = I_0 \exp(-\mu x) \tag{1}$$

where I is the recorded X-ray intensity, I_0 is the initial X-ray intensity, μ is the linear attenuation coefficient of the material, and x is the path length of the X-ray through the material. Eq. (1) only describes a homogenous material which, however, in natural samples is rarely the case. If the object is composed of several different materials, the linear attenuation of each material (u_i) as well as its linear extent (x_i) must be accounted for, resulting in the more general equation

$$I = I_0 \exp\left[\sum(-\mu_i x_i)\right] \tag{2}$$

In the case of a monochromatic beam this equation is sufficient to describe the attenuation of the X-ray beam through a heterogeneous object. However, the more typical laboratory setup employs a polychromatic X-ray beam. Because the linear attenuation coefficient μ is a strong function of X-ray energy, to describe X-ray attenuation of a polychromatic beam through a heterogeneous object requires solving Eq. (2) over the full X-ray spectrum

$$I = \int I_0(E) \exp\left[\sum(-\mu_i(E) x_i)\right] dE \tag{3}$$

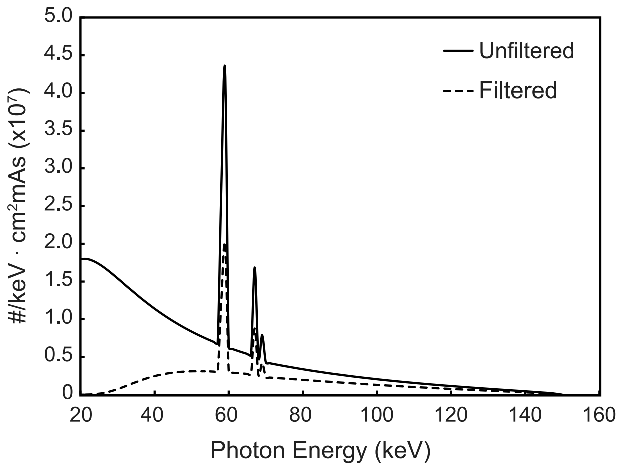

Fig. 1. X-ray energy spectrum generated from a tungsten target at 150 keV. Mean energy of unfiltered beam is 48.2 keV. Filtered spectrum represents same beam after filtering with 10 mm of aluminum. The filtered beam has a higher mean energy of 69 keV due to filtering of low energy X-rays. Graph produced using SpekCalc (Poludniowski et al., 2009).

In order to solve Eq. (3) the full shape of the incident X-ray spectrum is needed, but it is rarely directly measured and depends on several factors, including the target material and type (transmission or directional; Section 3.1), accelerating voltage, current, and any beam filters used (Fig. 1). These nuances make it difficult to accurately model a polychromatic X-ray beam, and therefore most reconstruction algorithms solve only Eq. (2), implicitly assuming a single effective energy. As discussed in more detail below, this mathematical simplification can lead to beam hardening artifacts within the reconstructed data.

Within the X-ray energies commonly used for tomography of planetary materials (<~450 keV), the attenuation of X-rays through a material is the result of three processes whose relative influence varies depending on the incident energy and material properties: photoelectric absorption, incoherent (Compton) scattering, and coherent (Rayleigh) scattering. During photoelectric absorption, an incoming X-ray photon liberates an inner-shell electron (which becomes a photoelectron) leaving the atom ionized. The original X-ray photon ceases to exist (i.e., it is absorbed). The probability of this effect is heavily dependent on the photon energy (Fig. 2) and the atomic number (Z) of the absorbing material, roughly to the fourth power $\sim Z^4$ (Als-Nielson and McMorrow, 2011). In Compton scattering the incident X-ray photon ejects an outer-shell electron (ionization) while retaining some of its energy and, as a result, is scattered as a lower energy photon (i.e., inelastic scattering) (Hsieh, 2009). The probability of this effect is dependent on the electron density of the material (Hsieh, 2009). This causes Compton scattering to be less sensitive to the material composition than the photoelectric effect, especially at lower energies (Fig. 2). The final process, coherent scattering, is an elastic process where the incoming X-ray photon causes an electron to vibrate at the same frequency and emit an X-ray photon of the same energy. The overall effect is that the incident X-ray is scattered but no energy loss occurs and the affected atom is unchanged (not ionized). The intensity of this effect is roughly proportional to Z^2 (Willmott, 2011) and is most pronounced at lower X-ray energies (Fig. 2).

The combination of these effects for different materials can be examined by plotting their total attenuation as a function of X-ray energy. The NIST XCOM database (Berger et al., 2010) compiles the X-ray attenuation coefficients (for scattering and photoelectric absorption, as well as total attenuation) for elements, compounds, and mixtures ($Z \leq 100$). We have created a tool in the form of a Microsoft Excel workbook called MuCalc (http://www.ctlab.geo.

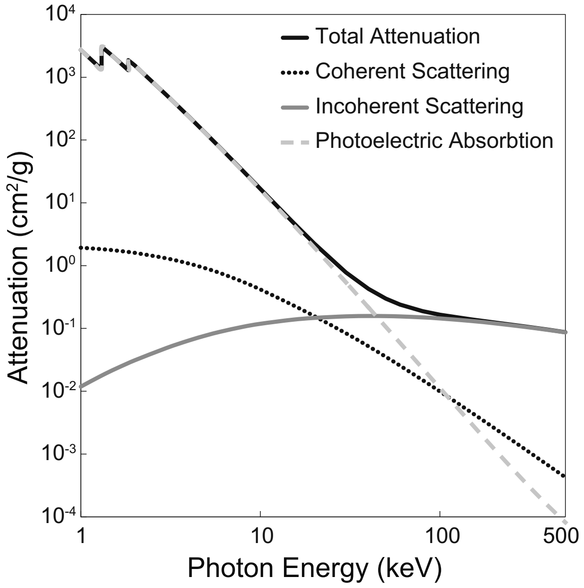

Fig. 2. Contribution of various X-ray interactions (coherent scattering, incoherent scattering, and photoelectric absorption) to the total mass attenuation of forsterite (Mg_2SiO_4) for energies up to 500 keV. Attenuation values from the NIST XCOM database (http://www.nist.gov/pml/data/xcom/index.cfm).

utexas.edu/software/) in which the total X-ray attenuations of various terrestrial and meteoritic minerals have been calculated using the NIST XCOM database and can be graphed in order to examine their relative attenuations at various X-ray energies (Fig. 3). Further details on this program can be found in Appendix A. The strong dependence of the photoelectric absorption process on Z, coupled with its dominance at lower X-ray energies (Fig. 2), makes lower X-ray energies more ideal for distinguishing certain minerals (for example, troilite and fayalite; Fig. 3). As the X-ray spectrum produced from a laboratory source is a complex continuum of energies up to the maximum energy (Fig. 1), the “effective” X-ray attenuation of the minerals in Fig. 3 is an integral of their attenuation coefficients at all energies in this range (Eq. (3)).

For the interested reader there are several books that provide more detailed treatments of the various aspects of X-ray computed tomography. A thorough mathematical foundation and detailed explanation of X-ray physics and interactions using both classical and quantum descriptions can be found in Als-Nielson and McMorrow (2011). Hsieh (2009) provides an overview of tube-based laboratory XCT including details on typical XCT system components, image reconstruction, and imaging artifacts. Buzug (2008) provides a similar overview but delves into cone-beam system components (albeit in a medical setting) and image reconstruction mathematics in considerably more detail. Those interested in synchrotron facilities for XCT are encouraged to consult Willmott (2011) for in-depth coverage of the capabilities, components, and operation of these systems, including information on additional analytical techniques available using synchrotron radiation.

2.3. *Really non-destructive?*

While XCT is described as non-destructive, X-ray energy is intimately interacting with material at an atomic level, notably by causing ionization and potentially heating. Therefore, some change is occurring at least on a subatomic level and the question arises of whether this interaction is causing a permanent change in material properties that are detectable using other analytical techniques. For meteorites and mission-returned samples where an irreplaceable specimen is often analyzed using a variety of techniques, potential sample modification from any one technique that could compromise the finding of another is a serious concern. In addition, the interest in using XCT as a general curation tool for planetary samples makes addressing this issue of critical importance to prevent large numbers of samples from being contaminated or modified in any way that potentially hinders future investigation.

For these reasons a few studies have emerged in recent years that aim to identify measurable changes in XCT-imaged samples. Ebel et al. (2009) calculated that the power deposited into 1 cm^2 sample cross section during a synchrotron imaging experiment at 10 keV would be $\sim 4.2 \times 10^{-4}$ W, which is many of orders of magnitude lower than the absorbed power from an electron microprobe and corresponds to heating 1 cm^3 of water by 1×10^{-4} degrees/s ($\sim 1°$ in 3 h). The University of Texas High-Resolution X-ray CT Facility (UTCT) tested for the effects of a routine laboratory XCT imaging experiment on the ferromagnetic remanence of two 25-mm-diameter terrestrial igneous (basalt) cores (R. Hanna and R. R. Fu, unpublished data). The two cores were first demagnetized in alternating fields (AF) of 85 mT. These cores were then imaged, one on our FeinFocus II system (180 keV, 0.22 mA; 83 mm source-object distance; 2.21 h acquisition) and the other on our Zeiss (formerly Xradia) microXCT system (90 keV, 10 W; 47 mm source-object distance; 0.98 h acquisition). Measurements of the remanent magnetization of the samples were made before and

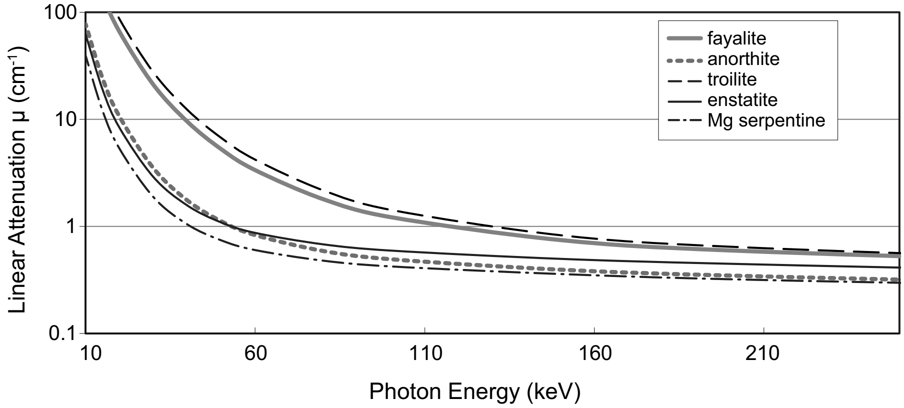

Fig. 3. Linear attenuation coefficients as a function of X-ray energy for common meteoritic minerals. Note the increased separation of linear attenuation for anorthite/serpentine and fayalite/troilite at decreased energies, and the change in relative attenuation between anorthite and enstatite. Anorthite is generally less attenuating than enstatite, but at lower energies (<55 keV) it is slightly more attenuating. At 55 keV they have equal attenuation and would be indistinguishable with XCT. Created with the MuCalc program (Appendix A).

after XCT imaging using the 2G Superconducting Rock Magnetometer at the MIT Paleomagnetism Laboratory. No change in the magnetic moment of the samples was detected after XCT imaging, implying that the change in the magnetization was <1% of the total moment. Reapplication of a 1.5 mT AF revealed no resolvable change in the magnetic moment; the maximum field to which the samples were exposed was therefore «1.5 mT. We conclude that XCT imaging using the settings indicated above lead to no significant magnetic contamination in our basaltic samples. In regard to organics, Ebel et al. (2009) investigated the effect of synchrotron tomographic imaging (beamline 13BM-D at the Advanced Proton Source; 12 keV for ~35 min) to polycyclic aromatic hydrocarbon (PAH) residue. No changes were detected in the PAH composition using laser-desorption laser-ionization mass spectrometry. Friedrich et al. (2016) tested for the modification of amino acids in two samples of the Murchison CM chondrite during conditions slightly harsher than routine synchrotron XCT imaging. They imaged the samples at 46.6 and 48.6 keV with longer beam exposure times (64 and 43 min, respectively) than typically used for microtomography imaging experiments and measured no difference in either the amino acid abundance nor the enantiomeric ratios (measured with liquid chromatography-fluorescence detection and time-of-flight mass spectrometry) after X-ray exposure. They estimated that the total dose experienced by two samples was ~1.1 kGy (kilograys) and ~1.2 kGy and also calculated that sample heating was negligible (<1° C).

However, Sears et al. (2015, 2016) did measure a significant rise in thermoluminescence (TL) in several ordinary chondrites after imaging the samples in a laboratory XCT system. They concluded that XCT-imaged samples experience a radiation dose of 85 ± 5 krad, which is consistent with the XCT dose calculation of Friedrich et al. (2016) (100 krad = 1.0 kGy). This dose is comparable to natural TL measured in Antarctic meteorites (<~100 krad) that results from a combination of cosmic ray exposure and internal radioactivity (Sears et al., 2013, 2016). Because the fall in natural TL during a meteorite's time on Earth is used to calculate its terrestrial residence time (e.g., Sears et al., 2013), XCT imaging could significantly complicate age determinations. Specifically, XCT-imaged samples could be mistaken for freshly fallen meteorites (Sears et al., 2015, 2016).

The confirmation of a measureable radiation dose for an XCT-imaged sample is unsurprising as X-ray radiation is ionizing in nature. It is expected that some molecular change is occurring as a result of this radiation, especially in the case of organics which have been shown to be more sensitive to ionizing radiation than non-organics, especially at lower X-ray energies (Bertrand et al., 2015). Indeed, Moini et al. (2014) examined the effects of synchrotron X-ray radiation on free amino acids [L-cystine, L-asparagine (Asn), and L-aspartic acid (Asp)] and confirmed that several molecular changes including modification (L-cystine; optically visible structure and color change), fragmentation (all), and racemization (Asp) occurred at low X-ray energies (8 and 22 keV). They found that the degree of damage increased when using a lower X-ray energy or a focused X-ray beam (i.e., beam focused to a smaller cross-sectional size with higher intensity) and for longer irradiation times (up to 1200 s). Likewise, the Stardust Team has verified that interstellar candidate grains, particularly organics, show evidence of radiation damage after exposure to synchrotron X-ray radiation experiments [X-ray fluorescence (XRF) and X-ray diffraction (XRD)] which use focused X-ray beams (Bechtel et al., 2014b; Simionovici et al., 2011). However, some damage appears to be the result of the particles being embedded in an insulating medium (Simionovici et al., 2011), and it is also unclear if similar radiation damage would occur when using unfocused beams for tomographic imaging. Because the unfocused beam widths are relatively large, the X-ray flux and resulting radiation dose is lower than the nm-scale beams achieved with X-ray focusing lenses (Bechtel et al., 2014a; Friedrich et al., 2016). Qualitatively, the authors and others in our laboratory (UTCT) have personally witnessed visible 'yellowing' of epoxy (for embedded specimens) that has been exposed to (unfocused) polychromatic X-rays (40–420 kV). The color change increases in intensity with repeated XCT imaging.

As a final note, we caution again that X-rays are physically interacting with matter to cause (permanent?) modifications at a subatomic level as a result of ionization and that further investigation, especially in regard to organics modification, is needed. While any changes may not be measureable with most analytical techniques commonly employed today, it is possible, even likely, that as technological advances to characterize material at increasingly smaller scales are developed, changes within matter exposed to routine XCT may become detectable. The potential impact of this scenario is impossible to know, but caution may be warranted when imaging samples at lower X-ray energies or with focused beams (e.g., Tsuchiyama et al., 2013), especially when preservation of organics is of particular concern.

3. Acquisition of XCT data

3.1. XCT system components

There are four primary components common among most non-medical XCT cone-beam systems: 1) an X-ray source that generates X-rays; 2) a rotating stage upon which the sample is mounted; 3) a detector that records the X-ray signal after passing through the sample; and 4) a computer that drives the system and records the collected data. The most critical components of a system are the X-ray source and the detector technology. In traditional turnkey laboratory-based tube XCT systems found today, polychromatic X-rays are generated from a finite point source and diverge to illuminate a sample volume. A cone of the X-ray energy is detected by a 2D planar detector composed of discrete elements, the number of which determines the maximum size of the final image (2048 × 2048 or 4096 × 4096 are common sizes today), although the data can be binned (multiple pixels averaged into a single pixel – see Section 3.3 for a more detailed explanation) to increase the signal-to-noise ratio (SNR), shorten acquisition time, and/or reduce data volume size. The sample is rotated through 180°(+fan angle) or 360° on the stage as a sequence of 2D X-ray projections (views) are recorded by the detector. These digital radiographs are recorded, stored, and ultimately reconstructed (Section 3.4) to produce a 3D volume of the sample's X-ray attenuation.

In addition to the energy spectrum generated (Fig. 1), other important parameters of an X-ray source are the intensity and the focal spot size. The intensity is controlled by the power input of the system and is often quoted as a maximum wattage. The greater the intensity, the better the SNR in the acquired data. The focal spot size is a major factor in determining the maximum spatial resolution that is achievable with a system and the amount of blur that will occur (see Section 3.2). In addition, the type of target (directional or transmission) determines the possible spot sizes and flux available. In directional targets the filament electrons hit a thick target material and X-rays are emitted from the target surface at an angle. In transmission targets the filament electrons pass through a thin film of target material and X-rays are emitted on the other side. Directional targets are capable of a higher flux but also have a larger spot size than transmission targets. Because of their lower flux and smaller focal spot size, transmission targets usually are only used for higher resolution (i.e., smaller object) XCT imaging.

The X-ray source energy, wattage, and focal spot size covary. The total power (wattage) of an X-ray tube is what ultimately governs the volume and type of materials that it can adequately penetrate. Power (P) is related to the energy (voltage V) and current (I) through:

$$P = VI \tag{4}$$

The operator can set the voltage (in kV) and current (in mA or μA) to produce the desired power (wattage), up to the maximum allowed on the system.[1] The spot size is inversely proportional to the power to prevent damage to the target. For example, if the system is run at a higher total power, the spot size is enlarged (defocused) to keep the total flux of electrons below a certain threshold, otherwise the target would overheat or crack (although a rotating anode can help limit overheating). Operation at a lower power (reduced voltage and/or amperage) allows for a more focused beam, producing a sharper but noisier image due to the lower intensity. In the end the particular settings used are primarily governed by the size and composition of the sample as well as the imaging objectives.

While a cone-beam source geometry is the most commonly employed today because of its relative efficiency and cost-effectiveness in X-ray generation and collection, its major drawbacks are a parallax effect around the upper and lower edges of the cone that leads to distortion at the edges of the field of view (FOV). This distortion can be minimized by ensuring that the system is geometrically well aligned or through the use of helical scanning, during which the cone beam is vertically translated through the sample during acquisition. This has the advantage that all portions of the sample are 'seen' by the nearly perpendicular central rays of the beam and the reconstruction algorithm can utilize this information to provide a more faithful geometric reconstruction of the object (e.g., Varslot et al., 2011; Yu and Xiaochuan, 2004). Systems capable of helical scanning are primarily limited to non-desktop XCT systems that can house the required gantry system, such as that at UTCT (http://www.ctlab.geo.utexas.edu/the-lab/).

Another way to avoid the common issues associated with a cone-beam geometry is to use a near-parallel beam that can be achieved using a synchrotron source (Ebel and Rivers, 2007; Fusseis et al., 2014; Kyle and Ketcham, 2015). This provides the minimal amount of geometrical distortion, but there may be limits to the FOV available and thus the maximum sample size (Ebel and Rivers, 2007). Yet another beam geometry is a fan beam configuration where the X-rays are collimated to a narrow horizontal beam that is recorded by a linear detector array. Although this requires vertical rastering through the sample (and therefore longer acquisition times), this is an ideal geometry for larger (dm-scale) objects that require higher X-ray energies to penetrate. Because attenuation of higher energy X-rays is dominated by scattering (Fig. 2), collimation to a fan beam and the use of a single row of detector elements minimizes associated artifacts (Kyle and Ketcham, 2015). A compromise that can be effective with a flat-panel detector is to collimate the beam and detector so that only a limited number of rows are illuminated, essentially gathering a "flattened cone" of data and eliminating the worst of the scattering.

The other important component of an XCT system that determines its performance is the detector. An X-ray detector is typically made of a scintillating material that produces photons of visible light in response to the absorption of X-ray photons. These flashes of light are counted and recorded by a device that digitizes the signal. Traditionally, charge-coupled devices (CCDs) are used, but these are gradually being replaced by thin film transistor (TFT) arrays (also referred to as flat panel detectors) which are generally regarded as superior technology (e.g., Jaffray et al., 1999; Seibert, 2006). Complementary metal-oxide-semiconductor (CMOS) chips can also be used and are generally lower in cost with faster frame rates but at the expense of image quality (noise). The quality of a detector for X-ray imaging depends on its size (both individual detector element size and the total number of elements), its efficiency in detecting X-rays (the ideal is 100% sensitivity to all X-ray energies), its ability to minimize cross-talk between detector elements, shadowing (i.e., image persistence or burn-in), and the speed with which it can record signals (i.e., latency). The last is the most limiting factor in how fast an X-ray projection can be acquired and therefore greatly influences the speed of the system. The physical size of the detector element determines how much of the object is subtended by it (i.e., the spatial resolution; Section 3.2) and the bit depth of a detector determines the number of different grayscale values it can record (i.e., the contrast in X-ray attenuation; high quality detectors today feature 16- to 32- bit depth).

3.2. Spatial resolution

The spatial resolution of a cone-beam XCT image is a function of several factors, including the imaging geometry, source, detector, and magnification optics if applicable. In the most general sense, the spatial resolution is a function of the width of the beam as it passes from the focal spot through the object to a detector element (Fig. 4a). The beam width is a function of the spot size (s), detector element size (d), the distance between the source and object (SOD), and the distance between the source and the detector (SDD) (ASTM E1441-11, 2011) (Fig. 4a):

$$BW = \frac{\sqrt{d^2 + [s(M-1)]^2}}{M} \tag{5}$$

where:

$$M = \frac{SDD}{SOD} \tag{6}$$

Because the X-ray spot has a finite minimum size, each detector element will collect X-rays that have gone through more than one path in the sample (Fig. 4a). It is easy to see from Eq. (5) and Fig. 4a that as the s increases, the width of the beam (BW) increases and thus spatial resolution decreases. The physical size of the detector elements also influences spatial resolution, as larger d will record more possible paths (larger BW). In the majority of systems d is large relative to the s and geometric magnification is used to vary spatial resolution by moving the object relative to the source (Fig. 4b). The highest resolution is achieved when objects are placed closest to the source and SOD (and therefore BW) is minimized. However, such an arrangement places the sample into a smaller region of the cone that illuminates the entire detector array, in turn limiting the field of view. Imaging small regions within larger objects is generally limited by the requirement to not place the sample so close to the sources that it hits it.

Conversely, some systems use optical magnification in addition to geometrical magnification (Fig. 4c). This reduces the dependence of the spatial resolution on the SOD and allows for high resolution and also higher magnification of subvolumes within large objects. In these systems the effective detector elements are smaller than the source and therefore objects are placed close to the detector (actually the scintillator; Fig. 4c) to maximize geometric magnification. The light from the scintillator is then optically magnified onto the detector to provide further magnification. XCT systems on synchrotron beamlines use optical magnification as well; the beam is nearly parallel, thus geometric magnification is not possible.

In both cases, a reasonable first-order simplification is that resolution in terms of voxel (volume element, or 3D pixel) size is simply the object width, or field of view (FOV) if a sub-region is imaged, divided by the number of elements across the detector array. For example, imaging an object 5 cm in size on a 2048 × 2048 pixel

---

[1] On some systems the two adjustable parameters are voltage and wattage. In this case the system auto-adjusts the current to supply the intended power.

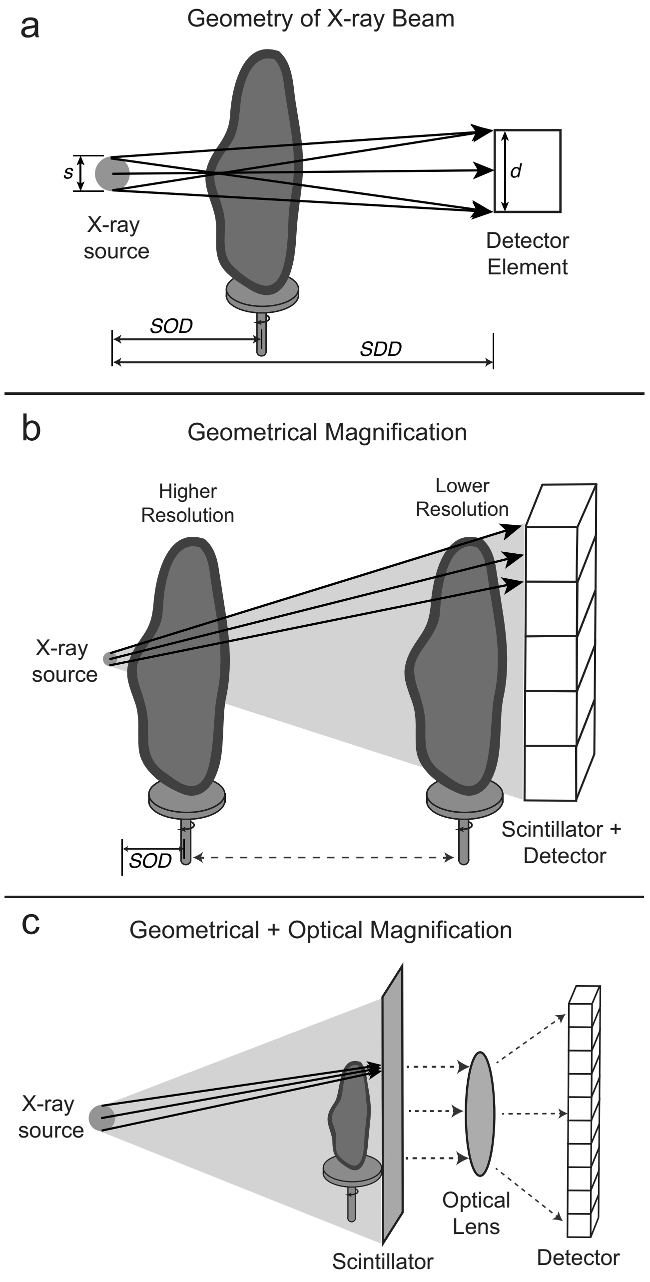

Fig. 4. X-ray beam geometry and magnification (a) The width of the beam path at the object defines the spatial resolution of an XCT image and is a function of spot size (*s*), detector size (*d*), source-object-distance (*SOD*) and source-detector-distance (*SDD*). Refer to Eq. (5) in text. (b) In geometrical magnification placing the object close to the source results in higher spatial resolution as *SOD*, and thus the beam width, is minimized. (c) On some XCT instruments the detector elements are small compared to the source and so the sample is placed close to the scintillator for maximum resolution. Optical magnification is then used to project light from the scintillator onto the detector. Optical magnification is also used in XCT instruments on synchrotron beam lines where a nearly parallel beam precludes geometric magnification unless zone plates are used.

detector results in a resolution of about 24.4 microns on a voxel edge, assuming the sample fills the entire FOV. However, resolution in terms of feature detection is also a function of the point spread function (PSF) of system (responsible for blur in XCT data (ASTM E1441-11, 2011)) which is a function of a number of factors including beam width, detector crosstalk, and precision of gantry motions. The PSF is discussed in more detail in Section 4.2.

3.3. *XCT acquisition parameters*

The optimal parameters for XCT acquisition are determined primarily by the sample composition and size and the research objectives. The spatial resolution of the data is often the primary concern, as it determines the ability to detect features of interest. In most cases spatial resolution does not directly correspond to feature detection, as it takes a few voxels to discern and measure a feature within an XCT dataset. Exceptions to this include when the material of interest has a markedly higher (e.g., metal) or lower (e.g., pore space) attenuation compared to the surrounding material, or a high aspect ratio (e.g., fractures). In such cases it may be possible to measure features, even on a sub-voxel level, by exploiting the partial volume effect (Kyle and Ketcham, 2015) (Section 4.2).

The other important variable in the design of an XCT experiment is the X-ray energy to be used. This also depends on the research objectives, specifically the materials that are present (e.g., minerals, voids) and which of these are important to distinguish in the data. A linear attenuation comparison tool such as MuCalc (Appendix A) can be valuable in determining the optimal energy to maximize the attenuation contrast between phases of interest (Fig. 3). While lower-energy X-rays are better able to maximize contrast between most minerals, they are also less penetrating, resulting in potential data contamination by noise or artifacts. The best compromise is to image at the highest energy that will still allow sufficient attenuation contrast between the phases of interest. If an energy below ~40 keV is required, a lower-atomic-number metal target (such as molybdenum) can produce better results, or a synchrotron source can provide the higher flux needed to avoid excessively noisy data. However, the penetration limitations of these lower energy X-rays will still require a relatively smaller sample and proper sample preparation. The ideal sample geometry is a cylinder, where the X-rays are passing through a consistent amount of material throughout the rotation.

In some cases, imaging the sample at two different energies (dual energy or absorption edge imaging) may be useful. Because the X-ray attenuation of a material is a well-defined function of its density, atomic number Z, and the X-ray energy (Fig. 3), imaging the same material at dual energies allows an estimation of its density and effective (average) Z (Van Geet et al., 2000). This approach requires careful calibration using materials of known composition and density (e.g., Alves et al., 2014) and complications from a polychromatic beam and beam hardening can limit success (Alves et al., 2014; Remeysen and Swennen, 2008; Van Geet et al., 2000). Another form of dual energy imaging (also referred to as absorption edge imaging) involves imaging a material at energies above and below its X-ray K-absorption edge (e.g., Ikeda et al., 2004; Ketcham and Koeberl, 2013; Mayo et al., 2015; Tsuchiyama et al., 2013). Because X-ray attenuation changes markedly on either side of the K edge for certain elements, the large attenuation difference can be used to identify and highlight materials composed of these elements (Ikeda et al., 2004; Mayo et al., 2015), even when using polychromatic sources (Ketcham and Koeberl, 2013). Careful selection of the X-ray energies and proper calibration of the system can also allow calculation of elemental concentrations (Ikeda et al., 2004) and mineralogical compositions (Tsuchiyama et al., 2013), although this requires a monochromatic beam (Section 5.4).

After the energy and spatial resolution requirements are determined, the rest of the imaging parameters are selected with the goal of providing sufficient quality data within a reasonable time. The more views (projections) that are collected during acquisition the higher the data quality, especially toward the periphery of the FOV. However, higher numbers of views will increase the acquisition time, especially on systems with detectors with a significant latency time, as well as increase reconstruction time (Section 3.4). Also, there are theoretical limits on the number of views which should be used (i.e., the Nyquist frequency; (Hsieh, 2009)) as well as practical limits to the increase in SNR (Uesugi et al., 2010). Improvement in SNR can also be achieved without incurring computational overhead by acquiring and averaging multiple frames per view. Another means of accomplishing the same effect is to increase the acquisition time per view, usually expressed in milliseconds. Again, the longer the acquisition time per view the higher the SNR, but at the cost of an increase in total imaging time.

Another way to increase SNR while decreasing computational overhead, but at a cost in resolution, is to bin the detector readings (sum signal from adjacent detector elements). For example, binning by two on an area detector will combine four pixels into one; assuming that the reconstruction size is also reduced accordingly, this will reduce the final voxel edge length by a factor of two and data size by a factor of eight. Although this decreases data resolution in terms of voxel size, to the extent that the true resolution reflects the beam width (Eqs. (5) and (6)) the actual information loss is often less, especially when using a defocused X-ray beam.

Another imaging option is to pre-filter the beam which will preferentially remove lower energy X-rays to decrease the effects of beam hardening and ring artifacts (Section 4.1), but this will also decrease the SNR and possibly degrade material discrimination, so care must be taken to not over-filter. The best choice for all of these parameters will vary depending not only on the composition and size of the sample but also on the particular XCT system and, in many cases, the budget (time and/or money). Hands-on XCT imaging experience is the best way to learn the most appropriate settings for various samples and instruments.

Finally, a series of careful calibrations must be performed prior to, during, and/or after XCT imaging to ensure data quality. The two most common are the dark field and bright field calibrations. A dark field calibration (also referred to as an offset) is a projection image taken while the X-ray beam is off. This is usually done only once, either prior to or after imaging, and helps to correct for detector bias present while the X-rays are off. The bright field calibration (also referred to as a gain) is taken with the X-rays on and the sample outside of the FOV; it is essential to correct for the differential response between detector elements, falloff (due to spherical beam), as well as to account for source drift (change in X-ray intensity over time). The timing of the bright field calibration(s) is generally machine-specific but will also depend on the imaging time (i.e. longer acquisitions can benefit from several bright field calibrations). Another calibration, which varies widely in its implementation among systems, is the geometrical calibration. This ensures that gantry motions are operating as expected, that the central rotation axis of the sample mount is at a known location with respect to the detector array, that the X-ray source and detector are properly aligned, and that the spatial magnification of the system is properly calibrated. For most turnkey systems a full geometrical calibration is performed during regular preventative maintenance visits and only a simple central rotation axis shift correction is applied during data processing for a an XCT dataset. However, for flexible-geometry systems (which can switch between linear, cone-beam, and helical scanning configurations or use multiple X-ray sources and/or detectors), a geometrical calibration is performed prior to each scan using a phantom (a machined part of known size and geometry).

3.4. Reconstruction

During reconstruction the XCT projections are processed and reconstructed into a 3D volume representing X-ray attenuation. The mathematical details of the reconstruction process are beyond the scope of this review, but the most common reconstruction algorithm is filtered back-projection (FBP) in which the data are first convolved with a filter and then the projections are 'stacked' onto a grid through their respective angular positions to gradually build an image of X-ray attenuation (Buzug, 2008; Hsieh, 2009). In its simplest form, FBP is used by systems with a parallel-beam geometry (i.e., synchtrotron source) (Fusseis et al., 2014). Cone beam XCT systems commonly employ the Feldkamp-Davis-Kress (FDK) algorithm, an extension of FBP that accounts for the 3D dispersion of the X-rays from a point source to a 2D detector (Hsieh, 2009). Reconstruction is a computationally intensive process. Unfortunately, most modern XCT systems come with their own proprietary reconstruction software that allows little flexibility in data processing/reconstruction and may employ behind-the-scenes algorithms that are not documented, such as noise suppression. Different convolution filters can be used to emphasize particular attenuation contrasts, resulting in improvements in spatial resolution or SNR, but usually as a tradeoff between one and the other (Hsieh, 2009; Ketcham and Carlson, 2001). Because pre-reconstruction data processing can greatly improve data quality (Section 4.1) and the computational demands of data reconstruction can create a bottleneck when imaging multiple samples, it is advantageous to use stand-alone reconstruction software that allows greater flexibility in the reconstruction process. Two options currently available are Octopus Reconstruction from Inside Matters (https://insidematters.eu/octopus) and the open source Astra Tomography Toolbox (http://sourceforge.net/p/astra-toolbox/wiki/Home/). A significant hurdle to this approach is translating the data from the instrument-produced format into something the reconstructor can understand.

The result of XCT reconstruction is a 3D image volume, which is typically exported as a series (stack) of 2D TIFF files, although other uncompressed image formats (e.g., BMP, DCM) or a 3D-format TIFF file may be used as well. The actual data values within the images are referred to interchangeably as CT values, CT numbers, gray levels, or gray scales, and represent the relative X-ray attenuation of materials within the object (see next section for complicating factors in this assumption). Because there is no standard byte scaling for non-medical XCT data, most reconstruction software allows the user to define minimum and maximum values between which the data are scaled (i.e., the histogram is spread between 0, or black, and 65535, or white, in the case of 16bit data). These can be selected to either encompass all data values (i.e., not saturate or truncate at either the low or high end, which is always the preference for quantitative work), or chosen to emphasize certain attenuation ranges within the dataset. It is not good practice to use byte scaling to eliminate the appearance of imaging artifacts. For example, scaling the data so that air in the FOV is a uniform black not only removes CT number variation that may alert users to the presence of imaging artifacts, but also shifts the apparent boundary of an object inward, compromising any measurements on the object.

4. XCT data

4.1. Artifacts

XCT data artifacts are variances in CT number that do reflect a material's actual X-ray attenuation and can significantly hinder data visualization and quantification if not properly accounted for. Some artifacts can be quite subtle and in some cases can significantly influence quantitative measurements, especially when dealing with objects that are small relative to the data resolution.

The most common (and frequently pernicious) artifact in tube-based polychromatic X-ray systems is beam hardening, which causes the CT number of a material to vary depending on its location within the data volume. This occurs because the lower-energy ("soft") X-rays are preferentially filtered out as they pass through an object, thereby "hardening" the beam and increasing its average

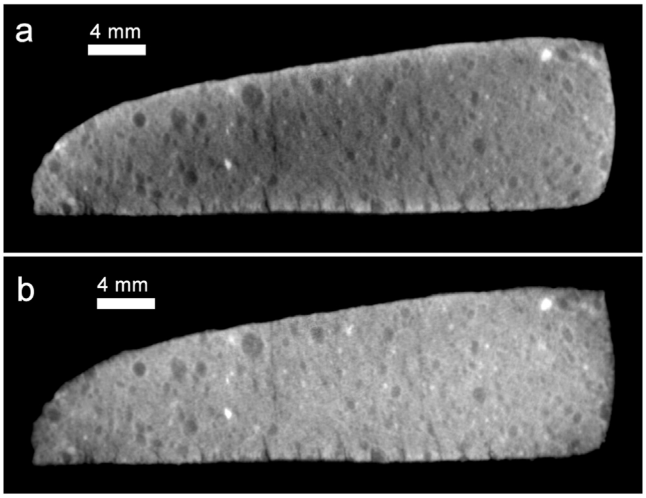

Fig. 5. Example of beam hardening correction using Ketcham and Hanna (2014). (a) CM Murchison XCT slice with beam hardening artifact. Note darker center and brighter edge, especially along top and bottom of sample. (b) Same XCT slice after beam hardening correction. The grey scales of the matrix are more consistent across sample and no central darkening is apparent. XCT data in both (a) and (b) has been corrected for rings (see Fig. 6a).

energy (Fig. 1). Because most reconstruction algorithms assume a constant energy (Eq. (2) in Section 2.2), this manifests as a gradual darkening toward the interior of the object (Fig. 5a) and is especially pronounced along the longest X-ray paths (Ketcham and Hanna, 2014).

Beam hardening can be prevented (best option) or corrected in a variety of ways, from the use of imaging calibrations and filters to post-acquisition data processing. XCT systems commonly employ beam filters of various materials to filter out lower-energy X-rays during acquisition of data and calibrations. However, this may lessen the effect without entirely preventing it. In addition, filtering the beam lowers its overall intensity, thus requiring longer acquisition times to achieve a given SNR. Using a phantom (a machined part of known size and geometry) of material with similar attenuation properties as the sample material can also help to minimize the effects of beam hardening, but requires unique phantoms for each type and geometry of sample imaged (Edey et al., 2013).

Due to the limitations of these preventative measures, a great deal of research has gone into post-acquisition data processing algorithms to eliminate beam-hardening artifacts. The first and still most commonly employed correction is a simple polynomial transform (usually 2nd to 4th degree) that attempts to convert the data from that of a polychromatic to a monochromatic attenuation response, a process referred to as linearization (Herman, 1979). This is the method used by most XCT instrument manufacturers today, as a single or multi-term input in the reconstruction software that is not always straightforward in its implementation and requires trial and error to find the best correction. Some of these shortcomings can be addressed using an iterative optimization process to find an optimal linearization function (Ketcham and Hanna, 2014); a correction using this approach is shown in Fig. 5. Another issue with linearization is that, while it might work well for homogenous materials or less attenuating biological samples, it is often insufficient for denser, heterogeneous objects such as geological specimens. More recent work has attempted to construct a correction that better approximates the X-ray attenuation of multiple materials imaged with a polychromatic beam (see Section 2.2 Eq. (3)), sometimes using an iterative approach to converge on a solution (e.g., Krumm et al., 2008; Kyriakou et al., 2010; Van Gompel et al., 2011). While promising, these algorithms are computationally expensive and remain somewhat limited in their applicability, though they are likely to be more widely available in the future as computational speeds increase (Section 6).

Other common XCT artifacts include rings, starbursts, shadows, and streaking, which unlike beam hardening are not limited to polychromatic X-ray sources. Ring artifacts are a result of the differential X-ray response of the discrete detector elements which, when combined with rotational data acquisition, manifest as rings (or partial rings) in 2D slice images (Fig. 6a). These can be prevented at acquisition by dithering the stage or the detector – shifting either by a few microns on X, Y and/or Z from one projection to the next – to average any variation in individual detector elements over adjacent channels. Post-acquisition, rings can be relatively straightforward to correct during data processing using the signals of surrounding detectors to average them out, even in reconstructed images (Ketcham, 2006b), but this processing can also introduce artifacts by modifying linear features that are tangential to the center of rotation (Kyle and Ketcham, 2015). Another common artifact, starbursts, are caused by highly-attenuating inclusions which leads to bright and dark streaks emanating from the inclusion into the surrounding area (e.g., De Man et al., 1999) (Fig. 6b). Shadowing (also referred to as photon starvation) is a similar phenomenon but can be more subtle, where darker areas form in the “shadow” of a highly attenuating material due to the extreme filtering of the beam in these ray paths (Fig. 6c). Shadowing can be quite difficult to avoid, even when using relatively high flux synchrotron sources (Ebel and Rivers, 2007). Finally, streaking is caused by very low SNR along long beam paths or the presence of highly attenuating material (Hsieh, 2009). This manifests as pervasive streaks across the reconstructed image [see Fig. 7.31 in Hsieh (2009) for an example].

4.2. *Partial volume effect and blurring*

There are two other artifacts inherent in all XCT data that cannot be corrected and must be considered in cases of segmentation or measurement of small features. The first is the partial volume effect (PVE), in which a single voxel contains more than one material and therefore its CT number is an average of the X-ray attenuation of all materials present. Intimately linked with the PVE is the general blur of XCT data, which can be quantified as a point spread function (PSF). The PSF describes the response of the system to an ideal point object and is a complex function of the beam width (*BW*; Section 3.2), detector response, system settings, and reconstruction algorithm (ASTM E1441-11, 2011; Ketcham, 2006a). This blur further complicates quantitative interpretation of CT numbers as it causes each voxel to contain contributions from the surrounding voxels. All material boundaries within a heterogeneous specimen will be subject to PVE and blur at some level due to the finite spatial resolution of an XCT image, but the issue will be most pronounced when the spatial resolution of the dataset approaches the spatial scale of the feature(s) of interest. For example, for a 15-μm thick vein imaged at 5-μm resolution the majority of voxels intersecting the vein will not reflect pure vein material, but some average of it and the surrounding material. Attempts to measure such features can be subjective and prone to both over- and under-estimation (Ketcham, 2006a). A reasonable solution is to image at higher resolution (see discussion of spatial versus feature resolution in Section 3.3) but this decreases the acquired volume, reducing the extent to which it is representative. Another solution is to account for this effect when measuring objects near the limit of the spatial resolution of the dataset, as implemented in some software such as Blob3D (Ketcham, 2005a) (Section 4.4).

Because the PSF is machine- and acquisition-dependent, it provides a way to measure and compare tomographic datasets among different machines/labs (ASTM E1441-11, 2011). This is useful because, while it has become standard practice to state the voxel size as a measure of precision, for features near the spatial reso-

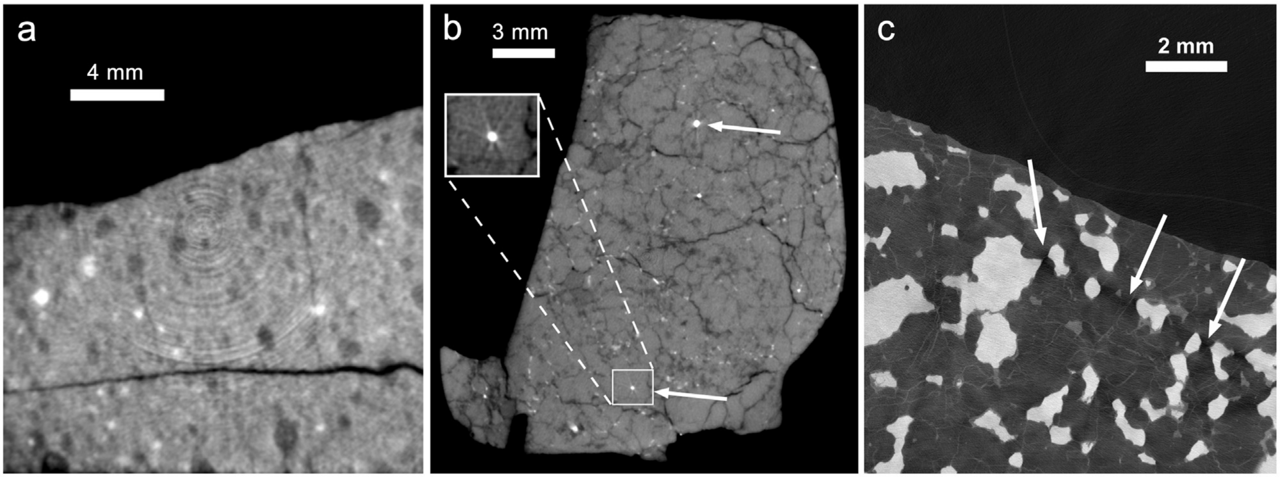

Fig. 6. Common XCT data artifacts. (a) Rings in CM Murchison XCT data. Beam hardening correction has been applied (see Fig. 5). (b) Starburst artifact (streaks) from metal inclusions in Almahata Sitta S138. (c) Shadowing from metal in lodranite NWA 2993.

lution the image's PSF may significantly affect the accuracy of this measurement (Ketcham and Hildebrandt, 2014). The PSF can be accurately measured using a software tool developed by Ketcham and Hildebrandt (2014) to provide greater confidence in the measurement of features (fractures, inclusions, pores) near the spatial resolution of an XCT dataset.

4.3. Visualization

The visual nature of XCT data allows even a novice user to interpret textural information within an imaged sample. The standard format that is most amenable to viewing with a variety of visualization software is a series of 2D images (slices) that can be loaded and 'stacked' into a 3D volume. Table 1 lists the most common commercial and freeware used for general visualization of XCT data. The list is by no means exhaustive. Because the determination of particular strengths and weaknesses of a program can be somewhat subjective, we include a few highlights of what we have found or have heard from colleagues to be unique about each program as it applies to XCT data.

The technological advances in XCT systems produce ever-larger datasets and a standard imaging experiment can produce a multi-gigabyte (GB) data volume. For this reason it is important to consider the computational requirements for XCT data visualization and measurement. Although some quantitative analyses require the native 16bit (2^{16}, or 65536 possible grayscale values) data depth that is typically output from the system, in most cases the data can be safely downsampled to 8bit (2^{8}, or 256 possible grayscale values) with a program such as ImageJ (Rasband, 1997–2015) to allow for faster manipulation and processing. It is also important to keep the data in an uncompressed (lossless) format such as TIFF or BMP rather than a compressed (lossy) format such as JPEG, which can significantly degrade data quality if used incautiously.

The basic visualization techniques easily done with a 3D XCT dataset are orthoslicing, isosurfacing, and volume rendering. An orthoslice is a 2D image that is orthogonal to the imaging geometry (the vertical axis of the sample on the rotation stage is Z). The original 2D images output by the instrument are the XY orthoslices perpendicular to the vertical rotation (Z) axis and standard 3D visualization software (Table 1) can be used to view orthoslices in the other two orthogonal planes (XZ or YZ). Most visualization packages can also reslice the data in any arbitrary orientation within the XCT volume, the output of which is usually referred to as an 'oblique slice' or 'nonorthogonal slice' in contrast to 'orthoslice' (Fig. 7b). An isosurface is a 3D contour within the data volume. Similar to a 2D topographic map line, an isosurface follows a particular CT number (grayscale) value within the dataset and can quickly highlight the exterior of a sample or a specific material or feature within it (Fig. 7b). Segmented phases (Section 4.4) can also be visualized as isosurfaces. Volume rendering is true 3D visualization, in which every voxel is assigned both a color and an opacity (Fig. 7a). Complex and stunning visualizations with false coloring and lighting can be produced using volume rendering, but creating a visualization that is both appealing and informative is an art. Fusseis et al. (2014) provides useful tips for creating visualizations from XCT data (see Section 3.4 and Appendix 4 in that work) and visualization textbooks such as Hansen and Johnson (2005) can be consulted for a more in-depth understanding on the various techniques.

4.4. Quantification

All of the visualization elements described above can be used to investigate and display the data in illuminating figures and animations, but the real power of XCT data lies in its potential for 3D quantitative analysis. An excellent, short overview of the process of quantification from XCT data is given by Jerram and Higgins (2007). The usual first step in any quantitative analysis is segmentation, in which sets of voxels are classified as particular phases of interest (e.g., minerals, porosity). There are many ways to segment data, and one major difference among different 3D analysis software programs is their segmentation capabilities (Table 1). In the simplest cases a global threshold (e.g., all voxels above a given CT number, or between two CT numbers) is used to isolate phases. However, more sophisticated segmentation algorithms are usually needed as the CT number of phases can be heterogeneous, overlap with other phases, or be subject to blur, partial volume effects, or other artifacts. There is a wide array of standard segmentation tools available today that include threshold-based (e.g., local thresholding, automatic threshold detection), region-based (e.g., watershed), or edge-based (e.g., graph-searching, Hough transform) algorithms (Sonka et al., 2014). More advanced segmentation methods that utilize machine-learning techniques include random walk and random forest (Breiman, 2001; Grady, 2006). The former is implemented in the SciKit Image toolkit (Table 1) and the latter is included in the Fiji plugin Trainable Weka Segmentation (Arganda-Carreras et al., 2016). Additional steps that may be required to facilitate segmentation of phases include pre-segmentation image

Table 1
Image processing and visualization software for XCT data.

Name	Commercial/Free	Highlighted Features and Comments
VGStudio	Commercial (Volume Graphics GmbH)	Intuitive graphical user interface and relatively easy to use after a gentle learning curve. One of the more expensive commercial visualization packages available, featuring superior volume rendering, lighting control and animation. Some image processing and segmentation tools but limited quantification capabilities.
Avizo	Commercial (FEI Company)	Shorter learning curve for creating simple but impressive visualizations. Superior image processing and segmentation tools compared to other commercial visualization packages, including 3D segmentation, separation, and measurement. Extensive user guide and documentation.
PerGeos	Commercial (FEI Company)	Based on Avizo and marketed toward the oil and gas industry. Includes all Avizo capabilities plus a variety of tools specific to rock core analysis including integration with core log data and a pore statistics and modelling module.
Imaris	Commercial (Bitplane)	Visualization and analysis package primarily geared toward the life sciences, but handles all volume datasets including microscopy data formats and 4D data.
Mimics	Commercial (Materialise)	Visualization and basic analysis software for medical data, including XCT. Widely used in the biology and palaeontology communities.
Dragonfly	Commercial (Object Research Systems Incorporated)	Newly developed XCT visualization software with excellent 3D rendering and extendable through user-developed python plugins and scripts. Software with full functionality available free of charge for non-commercial use.
Octopus	Commercial (Inside Matters BVBA)	Originally developed by Ghent University Centre for X-ray Tomography (UGCT) group. Standard 3D visualization capabilities but notably integrates with additional XCT reconstruction and data analysis modules. Data analysis module has filtering, segmentation, separation, and measurement (including discrete object orientation) capabilities. Standalone visualization module available as freeware.
ImageJ	Free (National Institutes of Health)	Excellent, stable analysis and visualization (although primarily 2D) open-source freeware with extensive documentation and very large user base. A must-have program for working with XCT data. A wide variety of specialized plug-ins are available. Volume rendering is weakly developed. Segmentation and measurement tools (mostly available as plug-ins) are somewhat limited and rarely operate in 3D.
Fiji	Free (National Institutes of Health)	An ImageJ bundle that includes many of the ImageJ plugins. Targeted at the life sciences.
Drishti	Free (Australian National University)	A more powerful freeware visualization package that includes flexible volume rendering and several other features for making impressive images. No user guide and little documentation make for a steep learning curve and somewhat hidden features.
Slice	Free (SPring-8)	Open-source freeware custom-built for XCT data visualization and analysis. A Unix environment and command line interface allow for building scripts.
Scikit Image	Free (scikit-image.org)	Open-source image manipulation library for the Python programming language. Contains many useful image processing tools, including advanced segmentation algorithms, that can be applied to XCT data. A tutorial for processing XCT data with scikit-image can be found at http://42eli.github.io
OpenCV	Free (opencv.org)	A powerful and heavily used image and video manipulation library for C++, C, Python and Java. Most of its capabilities are beyond that needed for XCT data but it contains advanced image processing tools that might prove useful for particularly tricky data. Its video processing library would also likely be useful for dynamic (4D) XCT (Section 6).

processing (e.g., filtering to reduce noise or minimize artifacts), post-segmentation image processing (e.g., to fill holes or remove false detections or 'islands'), and separation to make distinct objects of the same phase that are touching, if individual objects are to be measured. The software listed in Table 1 also vary in their image processing capabilities, from somewhat simplified (Avizo, ImageJ) to more sophisticated (SciKit Image, OpenCV).

Chondrules within XCT data of meteorites have proven to be particularly difficult to segment (Ebel and Rivers, 2007; Friedrich, 2014). Chondrules are usually polymineralic, with the same phases as the surrounding matrix material, and therefore are typically only distinguished by textural clues such as their large size, spherical shape, and/or differing grain size compared to the matrix (e.g., Griffin et al., 2012; Hanna et al., 2015; Lindgren et al., 2015). One promising technique uses local histograms of intensity to semi-automatically segment large components [including chondrules, Ca,Al-rich inclusions (CAIs), and dark inclusions] from the surrounding matrix (Griffin et al., 2012). This algorithm has been implemented into an open-source ImageJ plugin, PhaseQuant (Elangovan et al., 2012). Another recent technique allows for the segmentation of chondrules using sparse manual 2D segmentations of a chondrule in a minimum of three orthogonal planes (Hanna et al., 2015). The outer extent of all segmented orthogonal planes are then fit with an ellipsoid to derive size, shape, and orientation information for each chondrule. This enables rapid segmentation of chondrules while preserving the accuracy of segmentation and measurement (Hanna et al., 2015).

After segmentation and any additional processing are complete, various measurements can be made on the segmented entities using commercial visualization software (Table 1) or academically produced quantification freeware (Table 2). Among the latter is Blob3D which provides a rich set of object-based measurements including size, shape, surface area, projected area, CT number statistics, contact relationships, and orientation data (Ketcham, 2005a; Ketcham, 2005b). In addition it provides a mechanism for accounting for the PVE (Ketcham, 2006a) and characterization of the PSF (Ketcham and Hildebrandt, 2014). Quant3D characterizes pervasive 3D textural fabrics that are defined by distinguishable phases (e.g.,

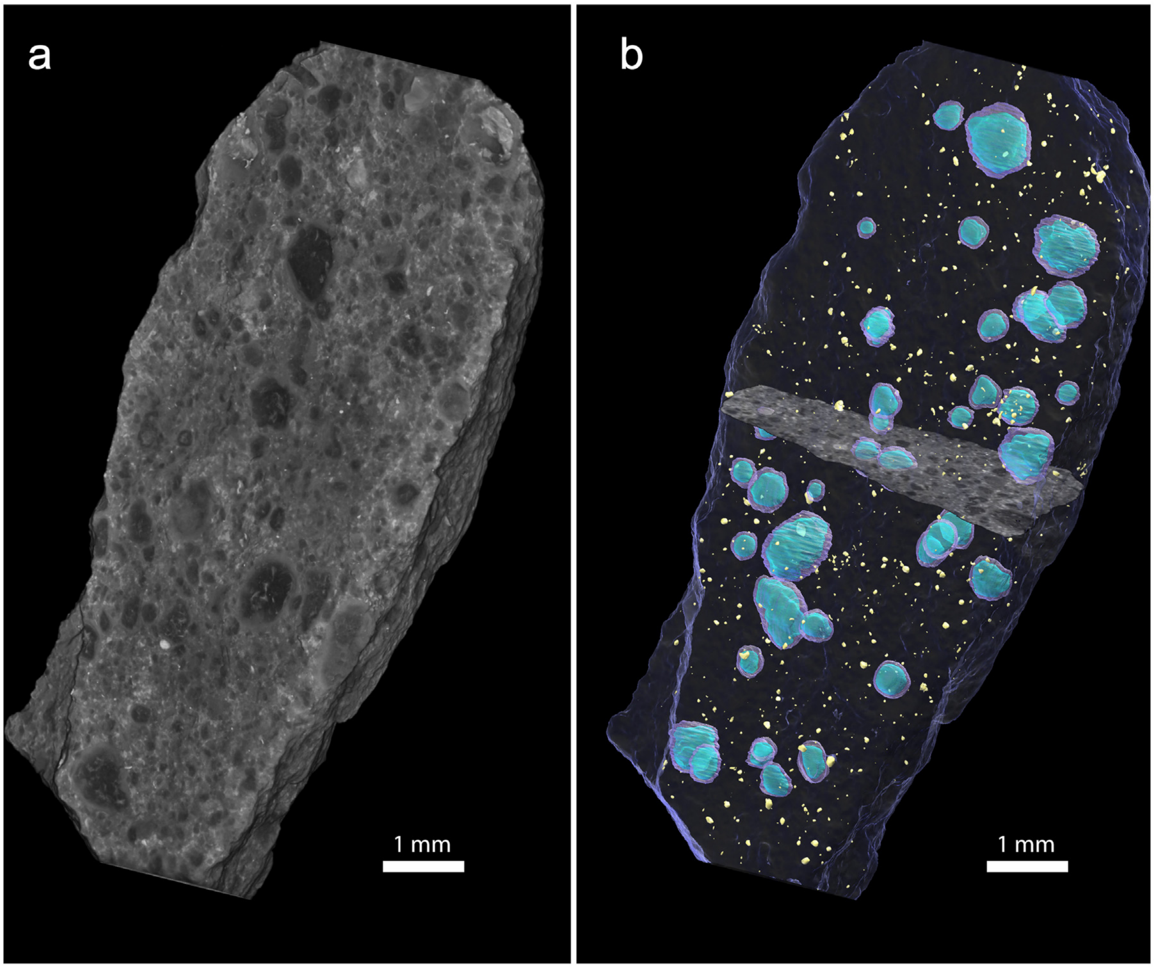

Fig. 7. 3D visualization of XCT data of CM Murchison. (a) Grayscale volume rendering of full dataset. (b) Isosurface of sample exterior is rendered as transparent dark blue. Fe sulfides and rare metal grains are rendered as yellow isosurfaces. A set of segmented chondrules (Hanna and Ketcham, 2015) is rendered as semitransparent isosurfaces. Light blue is chondrule interior and purple is surrounding fine-grained rim (FGR). Grayscale nonorthogonal slice is also shown near the center and intersects two segmented chondrules. Renderings were done in Avizo™ (FEI Company). (For interpretation of the references to colour in this figure legend, the reader is referred to the web version of this article.)

Table 2
Quantitative measurement freeware for XCT data.[a]

Name	Measurement Capabilities	Other Features	Download
Blob3D	Discrete object measurements: size, shape, projected area, surface area, primitive shape (ellipsoid) approximation, orientation information, CT number statistics, contact relationships	PVE correction, PSF measurement, image processing tools, segmentation and separation utilities	www.ctlab.geo.utexas.edu/software/
Quant3D	3D fabric orientation measurements using fabric tensors	Interactive 3D rose diagrams	www.ctlab.geo.utexas.edu/software/
PhaseQuant	Modal phase abundances and object size distributions	Access to other ImageJ utilities, segmentation module, ground truth tool, and density calibration module	http://geomodeling.uni-koeln.de/Geo-Cosmochemical_Modeling/PhaseQuant.html
Ctsta	Multiscale porosity, percolation and anisotropic permeability, including cluster analysis	Parallelized code can handle very large datasets	Contact developer at liujie86@mail.sysu.edu.cn
Slice	Discrete 3D object measurements: size, primitive shape (ellipsoid) approximation. Also modal analysis of binary data.	Image processing tools, command line interface and scripting	http://www-bl20.spring8.or.jp/slice/

[a] See Table 1 for commercial visualization software with more limited quantitative measurement capabilities.

minerals, porosity) within the sample (Ketcham, 2005b). PhaseQuant can calculate phase modal abundances (including porosity), object sizes, and provide an interphase distribution measurement, although it is currently optimized only for oxidized CV chondrites (Elangovan et al., 2012; Hezel et al., 2013a). However, PhaseQuant does provide a unique ground truth optimization feature that can estimate the measurement error on the modal phase abundances (Elangovan et al., 2012). Ctsta is a parallelized program that can analyze large segmented volumes to calculate multiscale porosity, percolation, and anisotropic permeability (Liu et al., 2009). Slice is a command-line UNIX-based program that can make discrete object measurements and calculate modal abundances (Nakano et al., 2006). Planetary studies utilizing the capabilities of some of these tools are discussed in the following section.

5. Applications in planetary science

We next highlight several recent applications of XCT to the study of planetary materials and analogs. Preceding reviews, including Ebel and Rivers (2007), reported on the earliest XCT investigations of planetary materials, so we will focus on studies published in the last decade or so. This includes an excellent special issue of *Geochimica et Cosmochimica Acta* in 2013 on the 3D imaging of planetary samples (Hezel et al., 2013b) from which several studies are highlighted.

5.1. Three-dimensional petrography

As a 3D investigation tool, XCT has enabled a new and powerful type of geological research – 3D petrography. Volumetric data encompass the complete specimen, unlike the limited characterization provided by thin sections, providing more opportunities for key observations. While mineral composition cannot be directly determined via XCT (except in special cases; Section 5.4), the combination of XCT data with traditional 2D microanalytical techniques (e.g., optical petrography, electron microbeam analysis) allows extrapolation to a 3D context. In addition, the unique 3D space of XCT permits the observation and quantification of petrographic textures and relationships only discernible in a 3D context.

One example of the 3D petrographic analysis possible with XCT is the study of two CV Allende and Mokoia chondrites by Hezel et al. (2013a), in which 3D modal abundances of chondrules and CAIs, compound chondrules, matrix, sulfide, metal, and porosity were derived using PhaseQuant with backscattered electron (BSE) images as ground truth data. The authors achieved a relative error of about 10% and, significantly, were able to separate the 3D modal abundances of metal and sulfide between chondrules and matrix. They interpreted the chondrule/matrix modal abundances with previously acquired Mg/Si ratio data to support chondrule-matrix complementarity and their formation from the same nebular reservoir. They were also able to view intrachondrule porosity and opaque-layered chondrules in both chondrites, and in observing a size dichotomy of opaques within chondrules versus the matrix, suggested that the latter were most likely not derived from the former as has been suggested for the CR chondrites (Connolly et al., 2001).

Needham et al. (2013) utilized XCT data to make several key observations of primary and secondary mineralogy as well as fracture networks within the Nakhla Martian meteorite. Unpolished sections from the XCT-imaged sample were used to examine fragile secondary phases (halite, sulfate, iddingsite) with an SEM. Then, after isolating the igneous host minerals of these phases within the XCT data, they were able to examine the 3D fracture network around them that enabled fluid flow for precipitation of the secondary minerals, including a gravitationally enclosed basin which provided a "way up" indicator for the meteorite's original orientation on Mars. They also calculated modal abundances of pyroxene, olivine, feldspar, and opaques on both a 2D slice and 3D volume basis, revealing that mm-scale heterogeneity could significantly influence "whole rock" geochemical analyses if not properly accounted for. Tomkinson et al. (2015) found similar modal abundance heterogeneity within another nakhlite, NWA 5790, by using XCT data. In this case the heterogeneity could be partially explained by the inhomogeneous distribution of olivine within the sample, easily visible as clusters in the 3D XCT data.

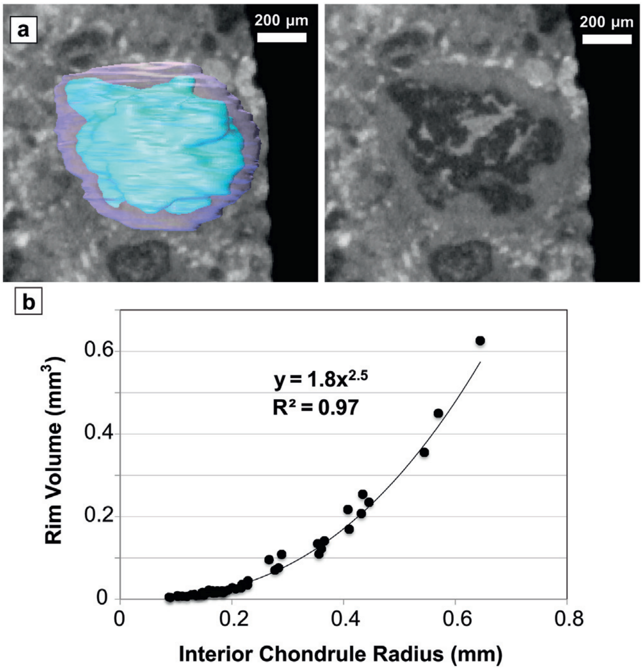

Fig. 8. Fine-grained rims (FGRs) in CM Murchison. (a) Example of a segmented chondrule and FGR. Image on left shows whole segmented chondrule with rim in purple and chondrule interior in blue bisected by XCT slice and the image on the right shows the XCT slice only. Scale bar the same for all images. The chondrule interior has a highly irregular shape but the exterior surface of the rim does not and is smoother. (b) Rim volume versus chondrule interior equivalent spherical radius. The data are well fit by a power law relationship, as proposed by Cuzzi (2004) for chondrules accreting dust rims in the protoplanetary nebula. (For interpretation of the references to colour in this figure legend, the reader is referred to the web version of this article.)

A recent application of XCT to 3D petrographic analysis is the measurement of fine-grained rims (FGRs) in the Murchison CM chondrite (Hanna and Ketcham, 2015). By imaging a small chip (143 mg) at relatively low energy (70 keV) and high spatial resolution (5.5 μm) they were able to discriminate the FGRs around chondrules due to their lower iron content relative to the surrounding matrix (Fig. 8a). Each chondrule was segmented twice (with and without the FGR), and their analysis showed that FGR volume is related to the interior chondrule equivalent spherical radius by a power law as proposed by Cuzzi (2004), strongly supporting a nebular formation model of FGRs (Fig. 8b). Work is ongoing to measure more chondrules to refine the power law fit and to examine the rim thickness in 3D to determine how the FGR may have been affected by deformation (e.g., Lindgren et al., 2015; Hanna et al., 2015).

Two other unique applications of XCT 3D petrography are an investigation of an interconnected plagioclase network in an H7 chondrite (Tait et al., 2014) and a survey of chromite inclusions among a suite of ordinary chondrites (Alwmark et al., 2011). Tait et al. (2014) demonstrated that large plagioclase crystals that appear isolated within 2D section are actually largely interconnected in 3D (Fig. 9). By quantifying the node coordination of the

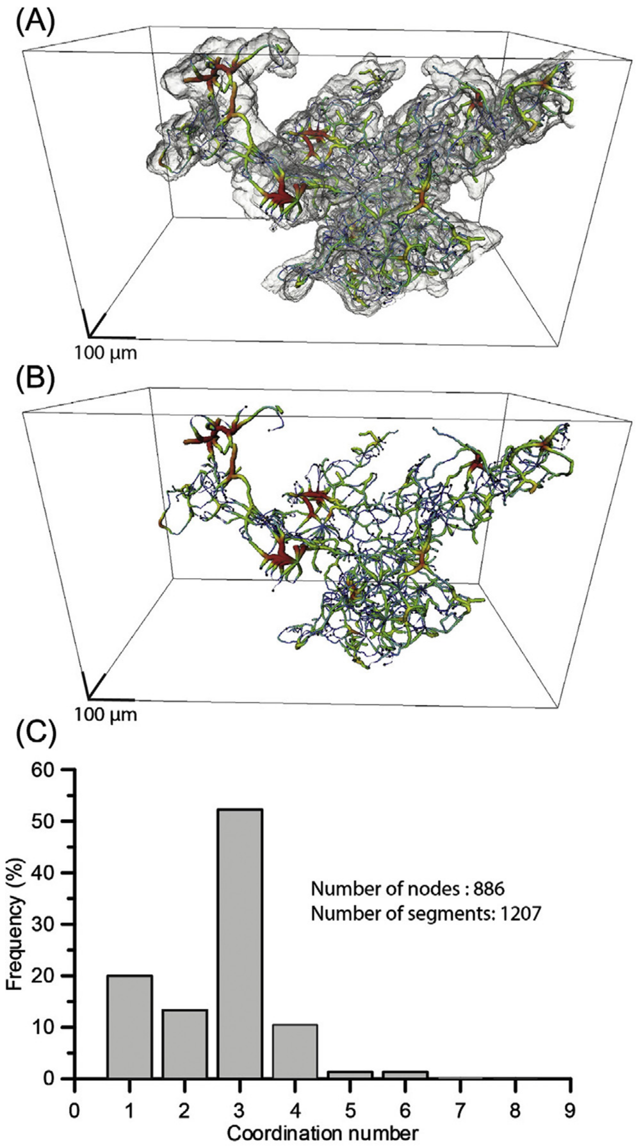

Fig. 9. Plagioclase network from XCT data of H7 ordinary chondrite Watson 012 from Tait et al. (2014). (a) Plagioclase rendered in grey over colorized skeleton network. (b) Colorized skeleton network where warmer colors emphasize thicker segments (wider plagioclase crystals). (c) Frequency distribution histogram of skeleton network in (b) showing that over 60% of nodes display coordination numbers of 3 or 4, consistent with a melt network in a grain-supported matrix. Figure reprinted with permission. (For interpretation of the references to colour in this figure legend, the reader is referred to the web version of this article.).

plagioclase using a skeleton diagram they found that over 60% of the nodes have a coordination of 3 or 4 (Fig. 9c), strongly suggesting that the plagioclase has pseudomorphed a grain-supported melt network. Alwmark et al. (2011) imaged the interiors of 385 chromite grains from 8 ordinary chondrites with synchrotron XCT to demonstrate that almost two-thirds of chromite grains contain inclusions and that the size and number of the inclusions as well as the size of the host chromite grains vary systematically with petrographic type. Further, the degree of fracturing of the host chromite is correlated with the assigned shock stage of the chondrite. Therefore, study of fossil extraterrestrial chromite grains (the most common mineral to survive long-term weathering on Earth) can provide information on the ancient meteorite flux to Earth.

Friedrich (2008) explored the quantitative possibilities of 3D petrographic observations of XCT data. He tested the use of the gray level co-occurrence matrix (GLCM) (Petrou and Garcia Sevilla, 2006) for the description and classification of chondrites and demonstrated that GLCM descriptors could statistically distinguish between equilibrated L chondrites (Akaba and Castine), an unequilibrated L chondrite (Gunlock), and an oxidized CV (Allende). He also investigated the use of Betti numbers to describe metal morphology in the L chondrites and proposed that they may be a useful metric to characterize metal morphological changes that occur with increasing degrees of metamorphism.

Another quantification metric that has been used for petrographic observations of chondrite XCT data is the chondrule convolution index (CVI). Originally proposed as a 2D thin section measurement (ratio of chondrule perimeter to the perimeter of a circle with the same area) by Zanda et al. (2002), later studies expanded the CVI to a 3D measurement using XCT (Ebel et al., 2008; Hertz et al., 2003; Nettles et al., 2006). Hertz et al. (2003) calculated both the 3D CVI and 2D CVI (using orthogonal slices in XCT data) for three Renazzo chondrules and found that neither measurement appeared to be a reliable indicator of the degree of melting or "chemical maturation" of a chondrule, as suggested by Zanda et al. (2002). Nettles et al. (2006) expanded this comparison of 2D to 3D CVI by randomly slicing an XCT-imaged Semarkona chondrule hundreds of times (including non-orthogonal directions) and confirmed that the range in 2D CVI (0.70) for a single chondrule was wider than the range proposed by Zanda et al. (2002) to represent different degrees of chondrule melting (0.69). Ebel et al. (2008) examined eight Renazzo chondrules in detail with XCT and 2D petrographic section. They also found that the 2D CVI measurement was an unreliable indicator but did find that the 3D CVI agrees with the "eye's intuition" of the extent of chondrule melting. They cautioned, however, that the measurement itself is somewhat subjective and could be more informative if combined with 3D metal grain texture and abundance. They illustrated the huge variation in 2D chondrule metal abundance and distribution compared to the true 3D values that are measureable using XCT data, strongly advocating for the use of 3D petrographic observations of chondrules when feasible.

5.2. *Petrofabrics*

Petrofabrics within geological materials provide textural information that can be used to infer deformational history and geologic setting. Terrestrial studies have the advantage of field observations and orientated samples so the structural geology of a large area can be investigated from field to microscopic scales. For extraterrestrial samples, similar structural studies are limited due to the lack of a larger spatial context and the relative rarity of material which restricts creation of the multiple orientated 2D sections required to measure a 3D fabric. As a 3D imaging technique, XCT overcomes the latter limitation and allows for investigation of structural fabrics on at least the hand-sample scale.

Due to their relatively high X-ray attenuation compared to less attenuating silicate minerals, metals can be easily segmented and measured in XCT data. An extensive study by Friedrich et al. (2008b) exploited this characteristic to measure several thousands of metal grains among a large suite of 25 ordinary chondrites using synchrotron XCT. Using Blob3D (Ketcham, 2005a; Ketcham, 2005b) they measured the size and orientation of the grains and found a strong increase in metal grain alignment with increasing shock stage (Fig. 10). This direct observation of metal grain alignment complements earlier work that used anisotropy of magnetic susceptibility (AMS) of metal to infer petrofabric development in increasingly impacted ordinary chondrites (Gattacceca et al., 2005).

Since their 2008 study, Friedrich and coworkers have used similar XCT methods to quantify metal grain shape and alignment in many other chondrites to infer their impact histories (Friedrich et al., 2013; Friedrich et al., 2014b; Gattacceca et al., 2014;

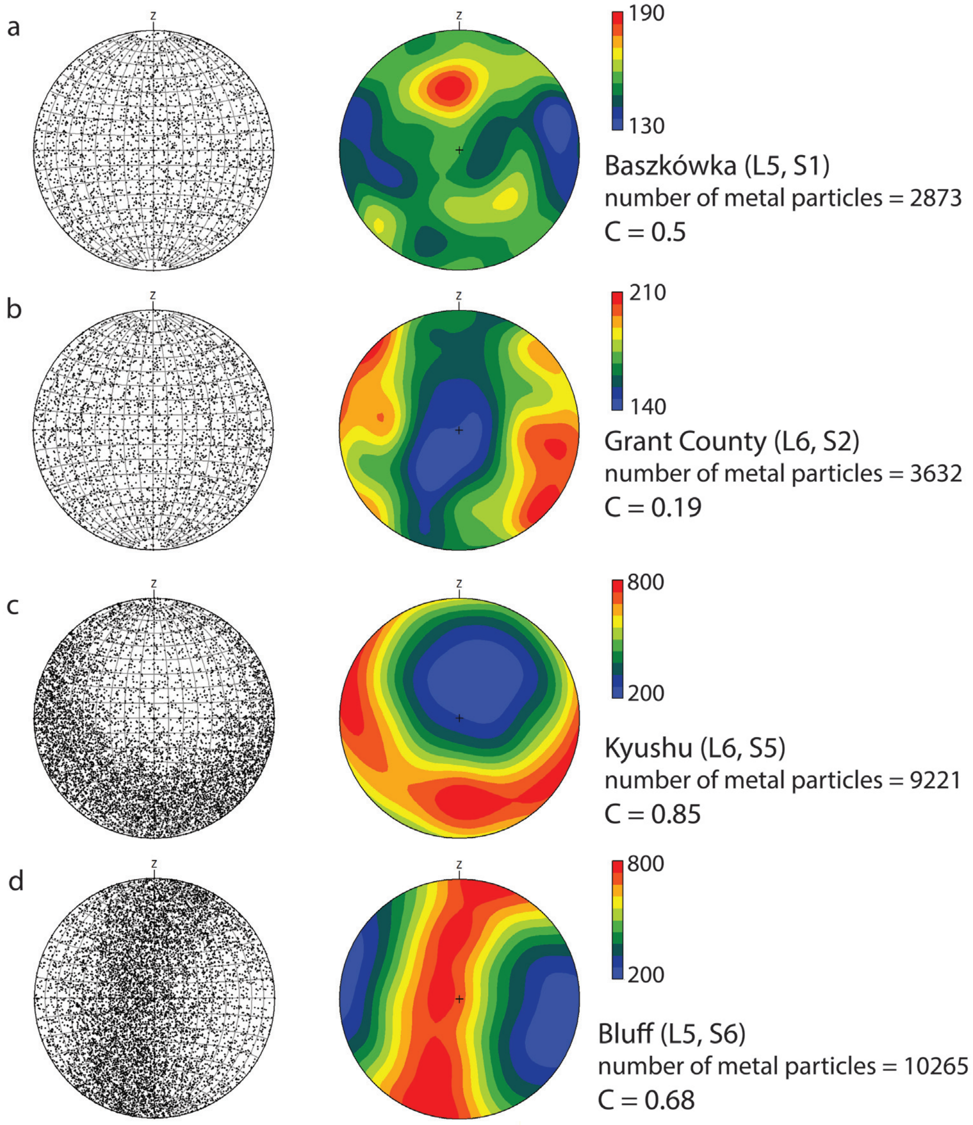

Fig. 10. Stereoplots of metal grain orientation in ordinary chondrites from Friedrich et al. (2008b). Metal grain alignment strength is quantified by C (grain number independent; higher numbers indicate stronger fabric) and generally increases with increasing shock stage for both L5 and L6 chondrites. Modified (courtesy of Jon Friedrich) from Fig. 4 of Friedrich et al. (2008b).

Jenniskens et al., 2014; Krzesińska et al., 2015; Popova et al., 2013; Zolensky et al., 2010). Friedrich et al. (2014b) demonstrated that an H chondrite breccia experienced multiple impacts of varying intensities. Through XCT and petrographic analysis they identified three separate lithologies within the sample with varying metal petrofabric strengths and orientations. They inferred that at least two impacts occurred on the parent body and that the variably impacted material was mixed together prior to the final impact. In another H chondrite, Kernouvé (H6), Friedrich et al. (2013) established that an early shock event occurred while the host rock was hot (pre- or syn-thermal metamorphism) and resulted in metal vein formation caused by shear stress which accumulated ductile metal grains along shear zones. The absence of a metal grain petrofabric in the chondrite further supported this interpretation, as thermal annealing likely erased any small metal grain alignment that occurred during impact and also reset the shock stage of the sample to S1. Ruzicka et al. (2015) found similar evidence for impact-shear-induced metal vein formation in the L6 chondrite Buck Mountains 005 using XCT. In addition, within the XCT data they found dextral shear sense indicators in the form of asymmetrical lenses within a metal-poor dike. The probability that these structures would have been found in 2D thin section is low, as it would have required fortuitously oriented sectioning.

Krzesińska et al. (2015) also found evidence for noncoaxial shear from impact using XCT. They surveyed 38 samples of the Pultusk H chondrite and selected three for higher resolution XCT imaging ($\sim$4.5–5.2 μm/voxel). The data revealed dark zones of cataclastic matrix with elongated metal nodules and bands that are aligned with shear indicators in the matrix. By comparing the XCT-derived metal modal abundances of the dark (low attenuation) matrix to the surrounding lighter (higher attenuation) clasts (Krzesińska, 2011), they determined that the metal concentrations in the matrix could be attributed to metal migration at the expense of smaller surrounding grains. They found a pervasive metal grain foliation and lineation within the meteorite, and showed that the clastic matrix had a significantly stronger fabric, consistent with the localization of noncoaxial shear strain within these zones.

Benedix et al. (2008) also examined a metal grain fabric, but one that was only indirectly caused by impact. The L chondrite PAT 910501 is an unshocked impact melt with vesicles, metal, and sul-

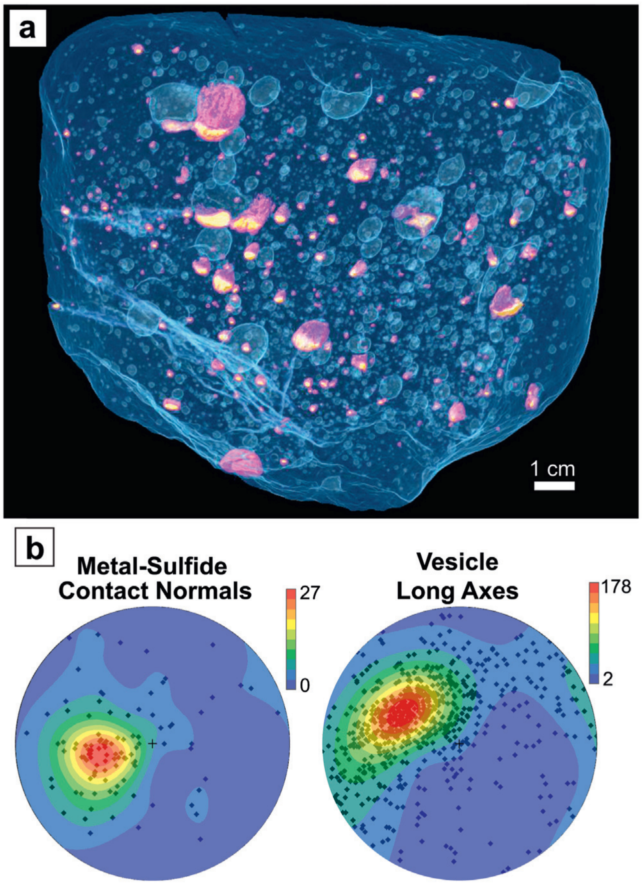

Fig. 11. (a) 3D visualization of XCT data of PAT 91501 from Benedix et al. (2008). Sample exterior and vesicles are rendered transparent blue, metal is yellow and sulfide is magenta. Specimen is orientated in implied crystallization orientation, with sulfide above metal, indicating gravitational orientation on parent body. Note that vesicles are elongated in a direction offset to the metal-sulfide contact (to the left in the image) (b) Stereoplot orientations in PAT 91501 from Benedix et al. (2008). Normals to planes of metal-sulfide contacts (left) and long axes of vesicles (right). Both are clustered indicating a preferred orientation. Orientation of metal-sulfide contact indicates gravitational direction in parent body during solidification of impact metal but the vesicle long axes are offset to this orientation. (For interpretation of the references to colour in this figure legend, the reader is referred to the web version of this article.)

fide grains, with the latter frequently in direct contact (Fig. 11a). XCT revealed a preferred orientation to both the metal-sulfide contacts and the vesicles, which were both clustered but offset relative to each other (Fig. 11b). Because the sample represents a relatively slowly cooled impact melt (Mittlefehldt and Lindstrom, 2001), they interpreted the orientation of the metal-sulfide contacts as an alignment to the local gravitational field as the sheet cooled. Further, the association of the larger vesicles with metal-sulfide intergrowths suggested that the vesicles formed via sulfur vaporization. The offset of the vesicles' long axes orientations to the metal-sulfide contacts was interpreted to result from minor melt turbulence, lateral melt movement that affected the vesicle orientations but not the metal-sulfide contacts, or the differing solidus temperatures of the metal and sulfide compared to the silicate melt which allowed for a gravitational vector change between their respective solidifications. Regardless, the XCT data provided a rare indication of the gravitational field orientation on the parent asteroid.

In addition to metal grains, chondrules frequently define petrofabrics in chondrites (e.g., Dodd, 1965; Martin and Mills, 1980; Rubin and Swindle, 2011). Because chondrules are typically composed of the same minerals (dominantly ferromagnesian silicates and phyllosilicates) as the matrix, they have similar X-ray attenuation and therefore cannot be as easily segmented as metal grains (Ebel and Rivers, 2007; Friedrich, 2014; Hanna et al., 2015). Friedrich (2014) suggests a novel, crowd sourced approach that proposes chondrule segmentation by a collective group of students who each process only a portion of the XCT data set. This allows for efficient, accurate segmentation of a few hundred chondrules in a single dataset while minimizing the time commitment of any individual researcher.

Despite the difficulty of chondrule segmentation, a few recent studies have examined chondrule petrofabrics in chondrites using XCT (Almeida et al., 2015; Hanna et al., 2012; Hanna et al., 2015; Lindgren et al., 2015). Almeida et al. (2015) manually segmented chondrules in XCT data of the Leoville CV chondrite and demonstrated that the 2D aspect ratio (measured from random 2D sections) consistently underestimates the 3D strain. The other studies (Hanna et al., 2012; Hanna et al., 2015; Lindgren et al., 2015) used orthogonal segmented sections (Section 4.4) to derive the shape and orientation of chondrules in the Murchison CM chondrite, with Lindgren et al. (2015) demonstrating again that the 2D aspect ratio underestimates the 3D strain. Lindgren et al. (2015) also found that the strain orientation indicated by the chondrule foliation differed from that derived by calcite *e*-twin analysis, which they attributed to multiple impacts. Hanna et al. (2015) found evidence for a weak lineation in addition to the foliation defined by deformed chondrules in Murchison. They used the petrofabric orientation measured in the XCT data to cut an oriented thin section from the Murchison sample and found evidence for multiple generations of brittle fracturing and other microtextures aligned with the foliation plane and lineation direction (Fig. 12a). They also found that some of the aligned fractures were filled with alteration minerals (serpentine and hydrated sulfide), strongly suggesting that aqueous alteration was contemporaneous with or post-dated the deformation events (Fig. 12b). Finally, they used the 3D aspect ratio of the deformed chondrules to estimate the finite strain experienced by Murchison and from this derived an estimate of pre-deformation bulk porosity of 32.2-53.4% [compared to the current Murchison porosity of 22.1% measured by He pycnometry (Macke et al., 2011)].

5.3. Porosity

Chondrite porosity is most commonly measured using ideal gas pycnometry (e.g., Consolmagno et al., 2008; Macke et al., 2011). However, this measures only bulk porosity and does not provide information on its location or morphology. And while 2D thin sections can be examined to obtain such information, sample preparation can also introduce secondary porosity that can be difficult to discriminate from primary porosity. These issues can be overcome by imaging porosity in-situ and non-destructively with XCT, although there will be a resolution limit below which porosity will not be discernible. Friedrich et al. (2008a) examined a porous (19%) L chondrite (Bsazkówka) using both He pycnometry and XCT and found that on average 64% of the pore space could be imaged and quantified with XCT at an image resolution of 16.8 μm. They estimated that only individual pores larger than $\sim 3 \times 10^{-5}$ mm^3 could be resolved, indicating that nearly two-thirds of the porosity is in the form of large inter- and intra-granular voids, which they interpreted as likely uncompacted, primitive porosity. Sasso et al. (2009) expanded the study to 5 more ordinary chondrites (LL, L, H) but imaged each chondrite twice: one sample at 16.6 μm resolution and a second sample of the same meteorite at 8.3 μm resolution. Unsurprisingly, they found that the higher resolution data was able to image more of the total porosity (up to 72%) compared to the lower resolution data (up to 51%) and, similar to Friedrich et al. (2008a), inferred that the majority of XCT-resolvable porosity in these relatively unshocked (S1–S2) chondrites is in the form of original uncompacted porosity, rather than impact-induced poros-

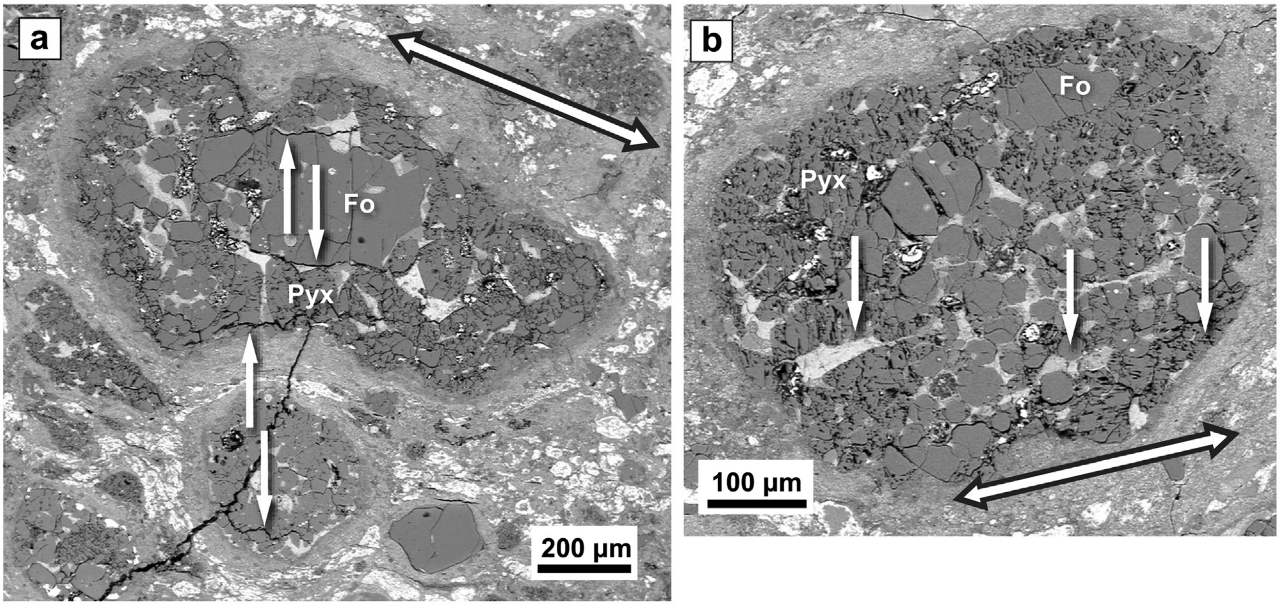

Fig. 12. BSE images of CM Murchison. Large black and white 2-way arrows designate orientation of foliation plane and lineation direction derived from 3D measurement of deformed chondrules in XCT data. Thin section was cut perpendicular to the foliation plane and parallel to the lineation direction. (a) Smaller chondrule is impinging upon the larger chondrule 'above' it and the implied compression direction is approximately perpendicular to the foliation plane. White arrows indicate fractures approximately (sub-) parallel to the petrofabric. (b) Chondrule is flattened in plane of foliation. White arrows indicate large Fe-Mg serpentine vein approximately parallel to the petrofabric. Modified from Fig. 10 of Hanna et al. (2015). Fo = Forsterite, Pyx = Mg pyroxene.

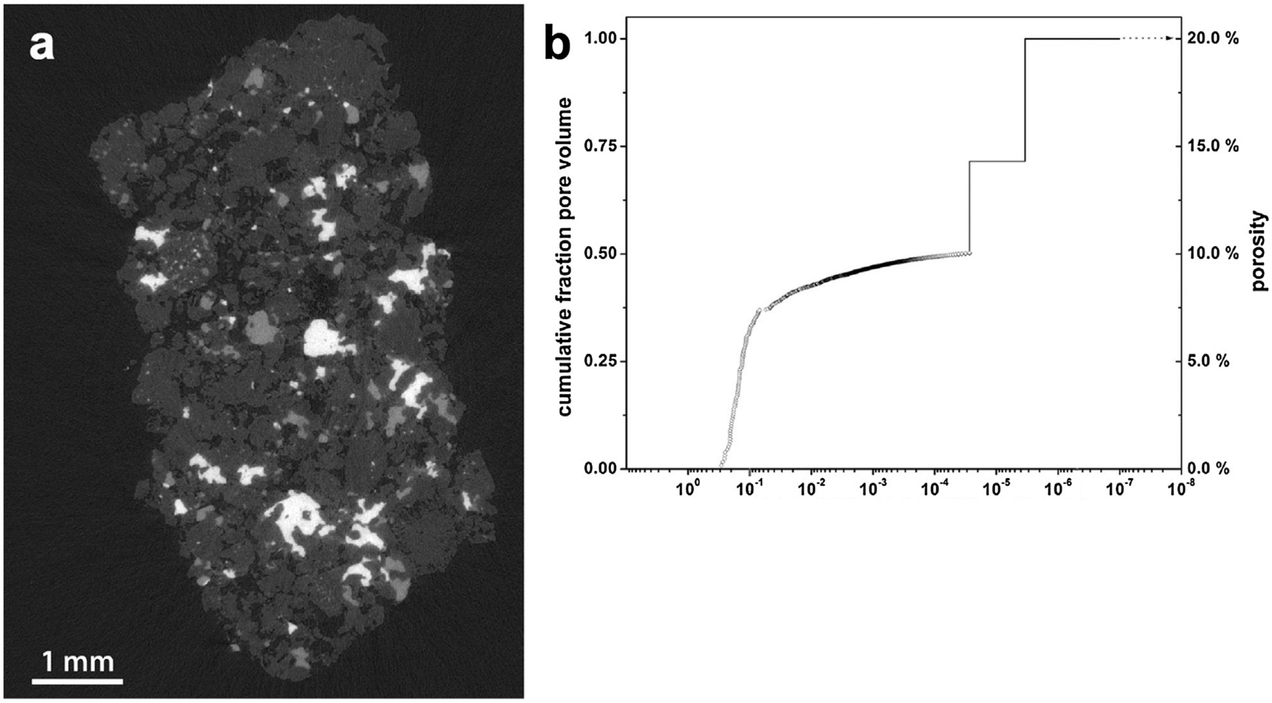

Fig. 13. Porosity of H5 Miller from Sasso et al. (2009). (a) XCT slice of uncompacted ordinary chondrite H5 Miller showing metal (nearly white), FeS (light grey), silicates (dark grey) and pore space (nearly black). Note the abundant large intergranular porosity. (b) Cumulative distribution of porosity in H5 Miller from He pycnometry and XCT. Individual pores were measured in the low-resolution XCT (16.6 μm) data but not the high-resolution (8.3 μm) data. Top limit of 20.0% porosity measured by He pycnometry. XCT is able to resolve ~51% and ~72% (low- and high-resolution XCT data, respectively) of the total porosity. Modified from Figs. 1 and 2 of Sasso et al. (2009).

ity (Fig. 13). Friedrich et al. (2014a) continued the study still further and found that while all 6 of these ordinary chondrites (OC), plus an additional LL chondrite (MIL 99301), were shock stage S1, they contained relict shock indicators. Based on ^{40}Ar-^{39}Ar dating and additional petrographic evidence of thermal annealing, they concluded that these chondrites experienced mild impacts into already hot material very early in OC parent body history, which produced relatively high shock features in silicates (subsequently annealed) while preserving a significant and rare amount of original, primitive porosity.

Friedrich and Rivers (2013) examined a suite of variously compacted/shocked ordinary chondrites at a resolution of 2.6 μm to determine the structural differences of microporosity among these chondrites. They demonstrated that XCT was able to resolve the vast majority of the microporosity in them (72–100%) at this scale. They also determined that the structure and location of microporosity has a regular relationship to the degree of compaction. Relatively compacted and shocked samples (Kyushu and Moorleah) retained the majority of their microporosity in the form of fractures and microcracks that are visible as sheet-like structures in the 3D data. In contrast, the microporosity of uncompacted samples (Bsazkówka and ALH A7725) is present as discontinuous intragranular and intergranular voids with little evidence of microcracks or fractures among the grains. This study demonstrated an important difference in the 3D structure of porosity among variably compacted chondrites that would have been impossible to characterize with bulk porosity measurements or more destructive 2D sectioning techniques.

Another unique approach to measuring porosity using XCT was done by Beitz et al. (2013a; 2013b). Rather than directly imaging porosity, these authors inferred its presence (at scales below the XCT data resolution) in planetary analog materials by calibrating the XCT grayscale values using nonporous material within the data. The first study (Beitz et al., 2013a) observed experimentally produced dust rims around chondrule analogs and derived porosity by examining the grayscale value between that of the pure analog material (zero porosity) and air (100% porosity). They then compared their results to porosity measured using backscattered electron (BSE) imaging of thin sections and found comparable porosity values between the two methods. Using these techniques, they determined that chondrule analog dust rims formed in a hot environment (1100° C) averaged 60% porosity, whereas rims formed at room temperature (20° C) had a porosity of 75%. They inferred that sintering processes were important in reducing the porosity of the hot accreted rim. They also illustrated their technique on a sample of CM Murchison, measuring a porosity of ~10% in two chondrule rims which is comparable to values reported in the literature. Beitz et al. (2013b) used XCT to estimate the porosities of 25 experimentally impacted analog chondrule(bead)/dust mixtures. As in the Beitz et al. (2013a) study, they estimated porosity by calibrating against the expected grayscale value of pure analog material with zero porosity. They found a sizeable range of maximum post-impact porosities, from 1 to 30% (initial porosities of the mixtures were calculated to be 39–70%), and the lowest porosities were achieved when the mixtures were 50/50 beads and dust. They also used the porosities of their impacted samples to calculate the pressures reached during compaction and inferred that the more porous CM chondrites were compacted and lithified at lower pressures than the less porous CV chondrites, confirming that the CMs are generally less shocked than the CVs.

5.4. Chemical composition and ultra-small particles

As discussed in Section 2, the linear attenuation coefficient (LAC) of a material is largely dependent on X-ray energy (Fig. 3) and therefore artifacts arise when reconstruction algorithms assume a single energy attenuation for data acquired using polychromatic sources. This severely complicates any attempt to use reconstructed CT numbers to derive the linear attenuation coefficient of a material (and thus the composition and/or density of the material itself). However, synchrotron sources can provide monochromatic X-rays that prevent these artifacts, allowing a quantitative relationship between CT number and theoretical LAC to be defined, especially for coarser grained material. Derivation of theoretical LAC values using fine-grained material will be more difficult as it does not account for variations in microporosity or grain boundary networks, which will also directly affect CT number. Still, Tsuchiyama et al. (2005) succeeded in this effort using the SP- μCT system at the SPring-8 synchrotron facility. By imaging a set of standards of known composition, they determined an empirical relationship between CT number and theoretical LAC and confirmed that the relationship held for several minerals in a garnet schist rock.

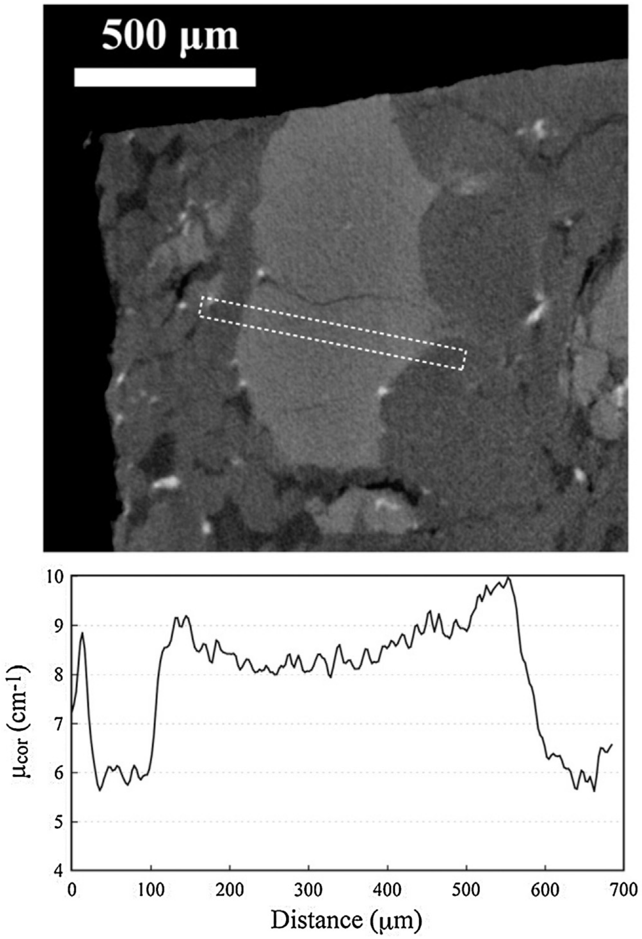

Fig. 14. Zoning in olivine phenocryst using LAC from Uesugi et al. (2010). (top) XCT slice of shergottite DaG 476 with olivine phenocryst. White dotted box shows location of LAC line profile (bottom). Plotted values are averaged perpendicular to the long side of the rectangle. Zoning in olivine is evidenced by its LAC variation from 8.1 to 10.0 cm^{-1} (center to rim), which is equivalent to Fa$_{29-39}$. Figure reprinted with permission.

Although specific to the SP- μCT system, this equation is independent of the material being imaged and has been successfully applied to the investigation of several meteorites. Uesugi et al. (2010) imaged a variety of meteorites (ordinary chondrites, CV3, CO3, shergottite, ureilite, and an iron meteorite) and demonstrated that the Fe content of olivine can be obtained and is comparable to the value obtained by SEM-EDS. They also demonstrated that subtle Fe/Mg zoning in an olivine phenocryst can be quantified using their LAC relationship (Fig. 14). They do point out that at the energies (≥30 keV) required to avoid noise-related artifacts in these 4–5 mm sized silicate and metal-bearing samples, the LAC values of some minerals overlap and thus textural observations are required to determine the mineral phase. However, with this information, chemical compositions of major minerals in meteorites can be determined, and general classification of meteorite samples is possible by using histograms of the LAC values present in an XCT dataset. Uesugi et al. (2013) applied the LAC method to a large suite of carbonaceous chondrites to further investigate the use of the LAC histograms to determine the chemical compositions of chondrules and matrix. They demonstrated that the peak LACs of both are correlated, indicating a compositional complementarity between them. They also extracted low-Fe inclusions (representing mainly chondrules, but also CAIs, amoeboid olivine aggregates (AOAs), and low-Fe silicate grains) and analyzed their size distributions, finding that they are unique among the different chondrite classes. Both of these findings supported localized formation of chondrites without large mixing in the nebula.

Motivated by the ambiguity of chemical composition in the LAC approach outlined above, Tsuchiyama et al. (2013) explored the use of analytical dual-energy XCT to more accurately determine mineral composition. This method was first introduced for the investigation of Hayabusa particles (Nakamura et al., 2011; Tsuchiyama et al., 2011) but a detailed description of the method is presented in Tsuchiyama et al. (2013). This method utilizes the LAC approach of Tsuchiyama et al. (2005) but images the sample twice at different energies, 7 and 8 keV, which are on either side of the Fe K-absorption edge. For Fe-bearing minerals, the LAC value will vary significantly between the two images, and the signature of this variation will be unique among different minerals (including Fe-bearing solid solutions), allowing more precise determination of the mineral phase and chemical composition. Fig. 15 shows an example of the dual-energy method on a heterogeneous Hayabusa particle. After imaging the particle, Tsuchiyama et al. (2013) mounted and polished the sample for SEM analysis and verified that the Mg# of olivine and low-Ca pyroxene matched EPMA results to within ~5% error. Due to the low energies (≤8 keV), however, there is a size limit of around 100 microns to the grains that can be analyzed using this technique (for imaging at the Fe K-absorption edge; if another element absorption edge is desired, the imaging energies and thus maximum particle sizes will change).

Because of the small sizes of the imaged particles, the dual-energy XCT technique requires higher imaging resolution (submicron) than is typical of standard XCT systems (>1 μm/voxel), even when using a synchrotron source (Wildenschild and Sheppard, 2013). To achieve this, an X-ray magnification optics system utilizing a Fresnel zone plate (FZP) was installed on a beamline at the SPring-8 facility (Uesugi et al., 2006). This system has been successfully used to image a variety of ultra-small particles at nanometer resolution (Section 6), including Hayabusa (Ebihara et al., 2015; Nakamura et al., 2011; Tsuchiyama et al., 2011, 2013) and Stardust (Nakamura et al., 2008a, 2008b) particles as well as organic nanoglobules from the C2 chondrite Tagish Lake (Matsumoto et al., 2013). Nakamura et al. (2008a, 2008b) achieved up to 43 nm resolution using the FZP setup to image several Stardust particles at 8 keV and examine the structure of both crystalline and amorphous particles. Nakamura et al. (2008b) also used the LAC relationship established by Tsuchiyama et al. (2005) to measure the Mg# of olivine in the crystalline particles and found that they were largely forsteritic (≥78 Mg#). Ebihara et al. (2015) measured the Mg# of olivine in Hayabusa particles using LAC analysis (84–96 nm resolution) and found that they are consistent with a composition of Fo68-Fo71. Matsumoto et al. (2013) imaged a particle of the C2 Tagish Lake meteorite at 42 nm and identified 38 organic nanoglobules (≤1 μm in size). They were not able to determine unambiguously whether they were hollow or fluid-filled, but they were able to confirm that none of them contained silicate (mineral grain) cores.

6. Future directions

The evolution of XCT is largely driven by advances in source and detector technologies that allow higher resolution and/or faster acquisition, or that provide new, complementary data modalities. In detectors, increased efficiency (in both speed and sensitivity) can significantly decrease measurement time per frame and facilitate time-resolved XCT experiments that can image dynamic processes in as little as one millisecond per projection, although the high brilliance of a synchrotron source is required (e.g., Armstrong et al., 2014; Mokso et al., 2011). Decreased detector element size and increased number of detector elements will also continue to see incremental upgrades. One of the latest innovations in detector technology is a hybrid pixel array detector (HPAD, also known as a photon counter) (Broennimann et al., 2006; Willmott, 2011). Unlike traditional CCD detectors, which accumulate a charge and then convert this into a digital signal, HPADs directly detect every single X-ray photon above a set energy, leading to a large reduction in background noise and thus greatly increasing SNR (Willmott, 2011). This new type of detector has already been installed at several synchrotron beam lines.[2]

Another active area of detector technology research is the development of X-ray detectors that can record the energy of the incoming X-ray photons, enabling chemical characterization (e.g., Egan et al., 2015). Currently there are two types of energy-sensitive detectors: 1) multispectral detectors that count single photon energies within each pixel and divide the detections into 5–10 energy bins; and 2) hyperspectral detectors that measure the energy accumulated in each pixel during an exposure time (frame) and subsequently reconstruct the pixel energy spectrum (Boone et al., 2014; Egan et al., 2015). The latter has the advantage of much greater spectral resolution but at a cost of measurement and processing time. Both of these detectors require a polychromatic X-ray beam and thus are well suited to laboratory-based XCT machines, although the detector technology has not yet been incorporated into commercial systems. However, Egan et al. (2015) demonstrated the potential for chemical characterization of a mineralized ore sample by replacing the standard flat panel detector in a commercially available laboratory-based XCT system with a HEXITEC hyperspectral detector (Fig. 16). As this detector technology matures it is anticipated that it will be added to commercially available XCT systems, opening up a myriad of avenues to explore 3D chemical composition in a laboratory setting.

Another way to derive 3D composition is to combine XCT with another analytical technique that can provide elemental or crystallographic information such as X-ray fluorescence (XRF) or X-ray diffraction (XRD) (e.g., Bleuet et al., 2010; Lemelle et al., 2004; Poulsen, 2004; Uesugi et al., 2013). The technique of combining XRF with XCT is further along but still limited in application as XRF tomography requires pencil beam rastering across the sample during each projection image resulting in significant acquisition times (Bleuet et al., 2010; Wildenschild and Sheppard, 2013). However, recent investigations utilizing position-sensitive X-ray spectrometers distributed around the sample stage have aimed to improve imaging speed (Meng et al., 2011). Still, fluorescence X-rays are prone to self-absorption and therefore typically only the outer few millimeters of a sample can be imaged (Wildenschild and Sheppard, 2013). In contrast, XRD has a penetration depth comparable to normal X-ray attenuation (Section 2.2), so combining XRD with XCT is more straightforward. In its most basic implementation, a pencil (focused) beam is rastered over the sample for each projection, but this necessarily leads to long acquisition times (e.g., Grant et al., 1994; Uesugi et al., 2013). For example, using XRD-CT, Uesugi et al. (2013) were able to image the distribution of olivine, serpentine, and pentlandite in a CM Murchison particle but only reconstructed a single slice due to the long experimental time (2 h for 1 slice). Much research has been done to create a true 3D tomographic XRD system that can map grain orientations in 3D using a non-focused, full-field beam (e.g., Grant et al., 1994; Herbig et al., 2011; Johnson et al., 2008; King et al., 2014; Ludwig et al., 2007; Poulsen, 2004). There are several variants of implementation, but X-ray diffraction contrast tomography (DCT) is unique in that simultaneous acquisition of diffraction data and absorption (XCT) are possible (Johnson

---

[2] https://www.dectris.com/references_list.html, accessed December 15, 2015.

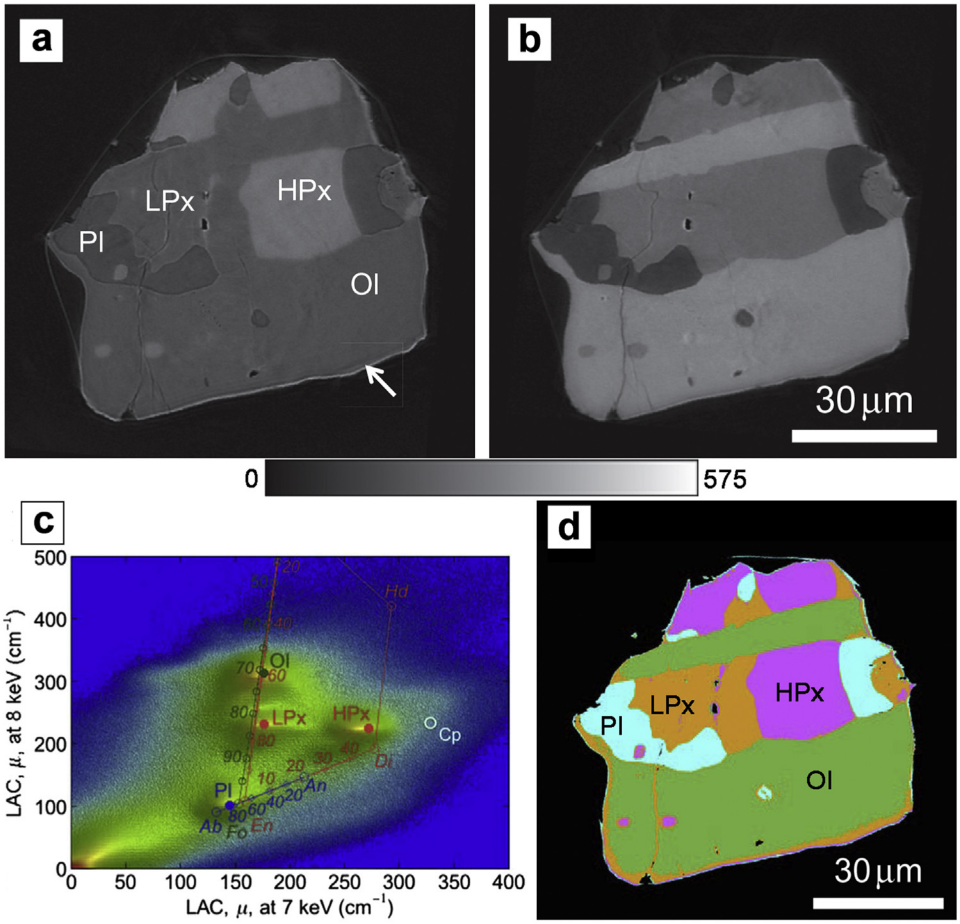

Fig. 15. Hayabusa particle RA-QD02-0024 from Tsuchiyama et al. (2013). (a) XCT LAC of particle at 7 keV. Arrow points to X-ray refraction artifact (phase contrast) at particle edge. (b) XCT LAC of particle at 8 keV. (a) and (b) have same scale and the greyscale bar indicates the LAC values of the images. (c) 2D histogram of LAC values at 7 and 8 keV; logarithmic density of the histogram is mapped to a rainbow color scale (bright blue is zero, red is maximum). Graph shows detail of silicate mineral LACs; metal and oxides plot outside this space. Numbers along the forsterite (Fo)–fayalite, enstatite (En)–ferrosilite, enstatite (En)–diopside (Di), and albite (Ab)–anorthite (An) lines are the forsterite, enstatite, wollastonite and albite contents (in mol.%), respectively. Ferrosilite and fayalite end members are just outside the plot area (above 500 cm^{-1} on the 8 keV axis). Large solid circles show LAC values calculated from the mean chemical composition of the minerals within the particle. (d) Mineral phase map determined by LAC analysis. Misidentifications are present at some surfaces, phase boundaries, and fractures. Ab: albite, An: anorthite, CP: Ca phosphate (F-apatite), Di: diopside, En: enstatite, Fo: forsterite, Hd: hedenbergite, HPx: high-Ca pyroxene, LPx: low-Ca pyroxene, Ol: olivine, Pl: plagioclase. Modified from Figs. 2, 4 and 5 of Tsuchiyama et al. (2013). (For interpretation of the references to colour in this figure legend, the reader is referred to the web version of this article.)

et al., 2008). Further, DCT can be done using a polychromatic X-ray tube source, enabling 3D crystallographic orientation mapping without the requirement of a synchrotron source (King et al., 2013) and is very recently available as an option on Zeiss Versa systems although it is currently only capable of mapping a mono-mineralic sample composed of a mineral with a cubic symmetry (i.e., metals) (Feser et al., 2015; McDonald et al., 2015).

There are several new developments in both laboratory and synchrotron X-ray sources that aim to increase flux, decrease spot size, and/or reduce heat on the target. For standard X-ray tubes, the latest advancement is the replacement of the solid metal target with a continuous liquid metal jet as the anode (e.g., Espes et al., 2014; Hemberg et al., 2003; Larsson et al., 2011). This allows increased power output (flux) even at smaller focal spots, as thermal damage or melting of the target material is not a concern (see Section 3.1). For synchrotron sources, development of the next (fourth) generation includes increasing the brilliance of the beam either through the use of an Energy Recovery Linac (ERL) or a Free Electron Laser (FEL), although the latter produces a destructive beam (Sham and Rivers, 2002; Willmott, 2011). The new fourth generation systems coming online in the immediate future (Max IV in Sweden and Sirius in Brazil) will also utilize multi-bend achromat magnets which can increase the X-ray brightness and coherent flux by 2–3 orders of magnitude (Bei et al., 2010; Reich, 2013). Several existing synchrotrons, including APS, SPring-8, and ESRF (European Synchrotron Radiation Facility), have planned upgrades using this new bending magnet technology (Reich, 2013). There is also active research intro shrinking the size of synchrotron sources to bring the brilliance of synchrotron radiation to a standard laboratory setting [i.e., Compact Light Source (CLS)] (Wildenschild and Sheppard, 2013; Willmott, 2011). These will not be as brilliant as current third-generation synchrotron sources, but will supply a flux somewhere between that of an X-ray tube and a storage ring beamline (Willmott, 2011). These are still in the development stage, although the first tomographic data utilizing a CLS have recently been acquired (Eggl et al., 2015).

Nanoscale XCT imaging (nanoCT), achievable at synchrotron sources for a decade (e.g., Nakamura et al., 2008b; Sakdinawat and Attwood, 2010), is now possible with laboratory-based sources. The first implementations utilized SEMs; directing the electron beam on a metal target produces an X-ray beam that can be used for full-field tomographic imaging of small samples (Vonlanthen

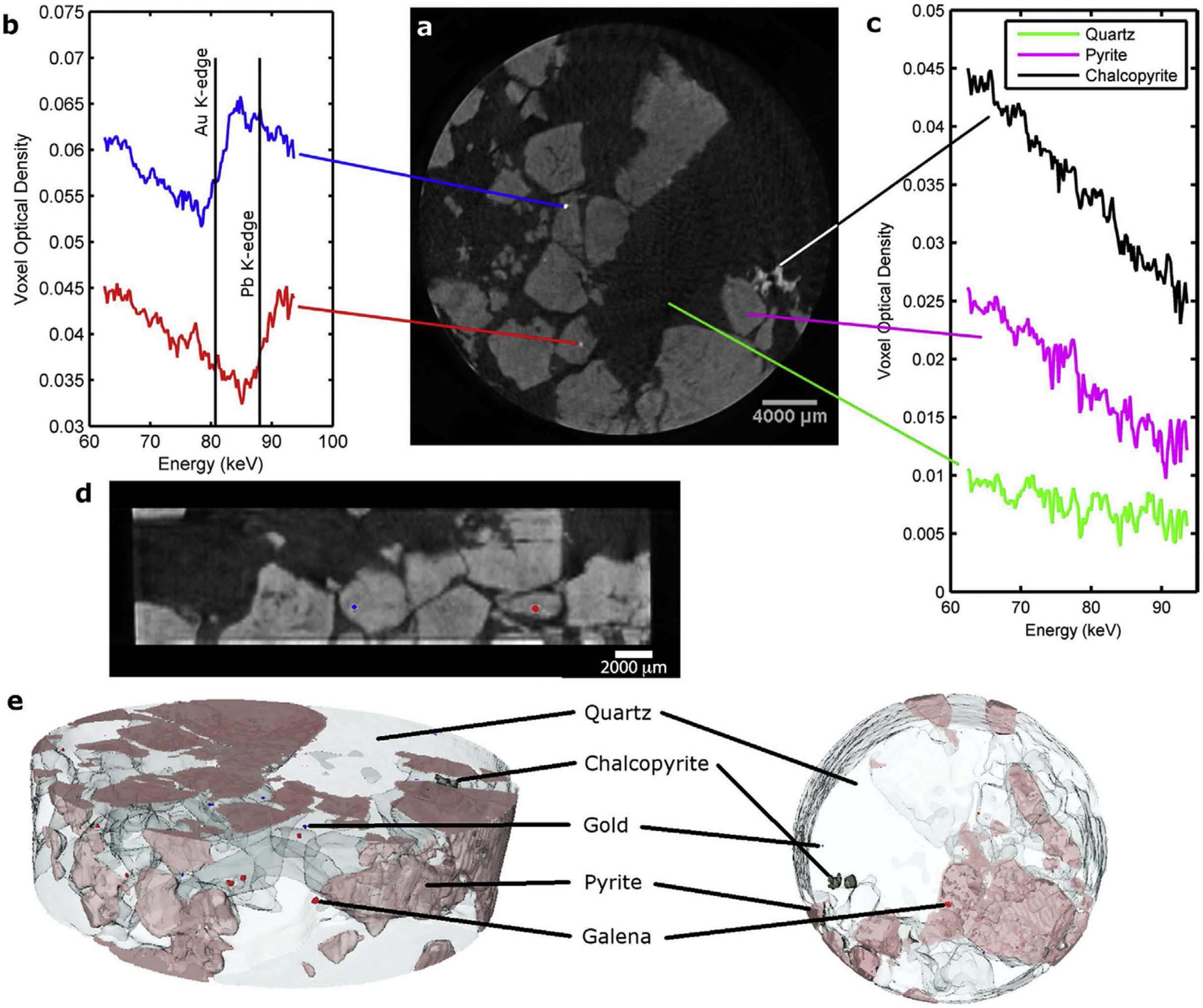

Fig. 16. XCT imaging using a hyperspectral X-ray detector. Sample is gold-bearing ore core. (a) 2D grayscale XCT slice of core. Grayscales represent integrated attenuation over full spectral range. (b) Single voxel spectra of two particles showing gold and lead K-edges. (c) Single voxel spectra of quartz, pyrite, and chalcopyrite. (d) 2D grayscale XCT reslicing perpendicular to imaging plane, highlighting segmented particles of gold (blue) and lead (red). (e) 3D visualization of core showing distribution of the various minerals. Modified from Fig. 3 of Egan et al. (2015). (For interpretation of the references to colour in this figure legend, the reader is referred to the web version of this article.)

et al., 2015). Although a theoretical resolution of ∼50–60 nm is reported, this requires specialized software corrections that are not widely implemented on commercial systems (Brownlow et al., 2006; Mayo et al., 2005). Actual implementations on commercial laboratory SEMs report resolutions an order of magnitude larger than this (∼500–600 nm) (Mayo et al., 2007; Russell and Howard, 2013; Vonlanthen et al., 2015). Russell and Howard (2013) imaged an unmelted CAI from the Allende CV3 chondrite at 550 nm resolution. The XCT data revealed that the CAI is a complex, porous network of rounded nodules, suggesting that it formed by condensation from a gas rather than from crystallization of a melt. Vonlanthen et al. (2015) imaged small volcanic ash particles also using an SEM-based XCT system. They included a detailed analysis and discussion of the actual spatial resolutions possible and concluded that, while the projection images have a resolution of ∼650 nm, mechanical instability, electron beam drift, and data processing can introduce significant blur into reconstructed images, making the practical spatial resolution (see Section 3.3) somewhat worse than this. These resolution limitations combined with long acquisition times [∼17–36 h; (Vonlanthen et al., 2015)] make their use somewhat limited, although future improvements in electron beam drift and mechanical stability should improve resolution (Mayo et al., 2007). For now, several commercial cone-beam laboratory systems can acquire data with similar resolution and faster acquisition times [see Fig. 1 in Maire and Withers (2014)].

The only true nanoCT (<100 nm resolution) laboratory systems commercially available today are the 800 or 810 Ultra systems sold by Zeiss. These systems utilize a high efficiency condenser lens and a Fresnel zone plate (FZP) to achieve a maximum spatial resolution around 50 nm (Tkachuk et al., 2007). They are also equipped with an annular phase ring that can be optionally inserted to produce phase contrast within the tomographic volume (Eastwood et al., 2014; Tkachuk et al., 2007). Phase contrast tomography is based on the refraction, as opposed to absorption, of X-rays at interfaces and so can highlight interior boundaries and edges (Eastwood et al., 2014; Wilkins et al., 1996; Withers, 2007). In fact, phase contrast effects are almost always present to some extent in XCT data from synchrotron sources due to the highly coherent beam (Cloetens et al., 2002; Fusseis et al., 2014).

Finally, ever-increasing advances in computational capabilities are driving development of XCT, mainly in the areas of reconstruction and data processing software. For example, increased processing speeds and the implementation of XCT reconstruction on GPUs (e.g., Fang and Klaus, 2007) are facilitating the use of iterative reconstruction (IR) algorithms, which are more accurate but computationally more expensive than filtered back projection (FBP) (De Witte et al., 2010; Hsieh, 2009). While FBP filters and projects the data only once, IR converges on a solution through repetition, requiring more computational resources (Beister et al., 2012). There is a myriad of types of IR algorithms and the recent review article by Beister et al. (2012) gives an informative overview of the major variants and recent developments.

These algorithms also enable reconstruction approaches that can produce high quality data from specialized XCT techniques such as discrete tomography and sparse imaging (Batenburg and Sijbers, 2011; Maire and Withers, 2014; Sidky et al., 2006). Discrete tomography aims to combine image reconstruction and segmentation in a single step, where the output of the reconstruction is a segmented data volume (e.g., Batenburg and Sijbers, 2011). This works well in situations where a few known homogenous materials are present and greatly simplifies the reconstruction iterations as the number of possible grayscales is limited (Batenburg and Sijbers, 2011). In addition, Myers et al. (2011) demonstrated how the simplified reconstruction of discrete tomography can enable time-resolved tomographic imaging of dynamic processes using two-phase fluid flow as an example. In sparse (or under-sampled) imaging, only a limited number of views are collected and IR algorithms have been shown to produce data superior to FBP in these situations (Chen et al., 2008; LaRoque et al., 2008). Sparse imaging is a particularly promising approach for XCT of dynamic processes in the laboratory where lower X-ray flux precludes the fast data acquisition possible with a synchrotron source (e.g., Mokso et al., 2011). Reconstruction with limited views would allow for faster data acquisition, perhaps on a timescale of some dynamic processes, although this has yet to be demonstrated (Maire and Withers, 2014). Finally, the general evolution of more powerful computers is enabling the development of more complex and/or automated XCT data segmentation algorithms such as Object Based Image Analysis (e.g., Leitner et al., 2014) and Iterative Local Thresholding (e.g., Deng et al., 2016).

7. Summary

X-ray computed tomography is an essential tool for 3D imaging at a wide range of spatial scales, with increasing improvements in technology enabling nanometer-scale resolutions and time-resolved experiments even in a laboratory setting. It has been applied with great success to address many problems in planetary science and the expectation is that its use will only grow as the technique becomes more widely available and adopted. Its exceptional capabilities for 3D visualization and quantification have been amply demonstrated, and future developments, most notably the integration of XCT with other techniques that can be used to determine chemistry and/or mineralogy, will greatly expand its utility. Certainly, XCT is quickly earning its place among the standard analytical techniques available today to study planetary materials.

Acknowledgements

We gratefully acknowledge many long and enlightening discussions regarding all aspects of XCT with the entire UTCT team: Dr. Jessie Maisano, Dr. Matt Colbert, Dave Edey, and Gary Zuker. Jessie Maisano and Dave Edey provided early detailed reviews of the manuscript that greatly improved its clarity. Thanks for Roger Fu for help with the magnetics test. The University of Texas at Austin UTCT facility was created with support of the W.M. Keck Foundation, the National Science Foundation (EAR-9406258), and the Geology Foundation of the Jackson School of Geosciences at the University of Texas at Austin. Continuing support for lab operations as a multi-user facility and for software development is also provided by NSF (EAR-1561622, EAR-1258878, EAR-0948842, EAR-0646848, EAR-0345710, EAR-0113480, EAR-0004082, EAR-98160200). R.D.H. is supported by the NASA Earth and Space Sciences Fellowship Program – Grant NNX13AO64H. This Invited Review was solicited and handled by Associate Editor Klaus Keil.

Appendix A.

MuCalc is a Microsoft Excel workbook that can be used to compare the X-ray attenuation of various minerals. A mineral's X-ray attenuation is primarily determined by its chemical formula and density, and the key to distinguishing between different minerals in a rock using XCT is to image at an energy where each mineral has a different X-ray attenuation (if possible). This workbook allows a user to determine if the various minerals in their sample will be distinguishable in the XCT data, and if there is an optimal energy at which to image in order to maximize their relative differences in attenuation. Within the workbook, the user selects the constituent minerals from a drop-down list and their X-ray attenuation versus energy (up to 500 keV) are plotted together on a graph (see Fig. 3 for an example). The mass X-ray attenuation coefficients for the minerals in the workbook were retrieved using the NIST XCOM database at http://physics.nist.gov/PhysRefData/Xcom/Text/XCOM.html, and the coefficients are multiplied by the mineral's common density to obtain the final X-ray attenuation values.

The workbook currently contains a list of ~250 common terrestrial and extraterrestrial minerals and native elements but detailed instructions are included on how to add a new mineral or element. In addition, there is a solid solution tool that can be used to define a new solid solution mineral out of existing minerals in the workbook and to add this to the permanent mineral list. MuCalc can be downloaded at http://www.ctlab.geo.utexas.edu/software/

References

Almeida, N.V., Smith, C.L., Sykes, D., Downes, H., Ahmed, F., Russell, S.S., 2015. Quantifying the deformation of Leoville chondrules in 3D: Implications for the post-accretional history of the CV3 parent body. In: 78th Annual Meeting of the Meteoritical Society, Berkeley, CA, #5112(abstr.).

Als-Nielson, J., McMorrow, D., 2011. Elements of Modern X-ray Physics, Second ed. John Wiley & Sons Ltd, Singapore.

Alves, H., Lima, I., Lopes, R.T., 2014. Methodology for attainment of density and effective atomic number through dual energy technique using microtomographic images. Appl. Radiat. Isot. 89, 6–12.

Alwmark, C., Schmitz, B., Holm, S., Marone, F., Stampanoni, M., 2011. A 3-D study of mineral inclusions in chromite from ordinary chondrites using synchrotron radiation X-ray tomographic microscopy—method and applications. Meteorit. Planet. Sci. 46, 1071–1081.

Arganda-Carreras, I., Kaynig, V., Rueden, C., Schindelin, J., Cardona, A., Seung, S.H., 2016. Trainable_Segmentation: Release v3.1.2., http://dx.doi.org/10.5281/zenodo.59290.

Armstrong, R.T., Georgiadis, A., Ott, H., Klemin, D., Berg, S., 2014. Critical capillary number: Desaturation studied with fast X-ray computed microtomography. Geophys. Res. Lett. 41, 2013GL058075.

Arnold, J.R., Testa, J.P., Friedman, P.J., Kambic, G.X., 1983. Computed tomographic analysis of meteorite inclusions. Science 219, 383–384.

ASTM E1441-11, 2011. Standard Guide for Computed Tomography (CT) Imaging. ASTM International, West Conshohocken, PA, http://dx.doi.org/10.1520/E1441-11.

Batenburg, K.J., Sijbers, J., 2011. DART: a practical reconstruction algorithm for discrete tomography. IEEE Trans. Image Process. 20, 2542–2553.

Bechtel, H.A., Flynn, G.J., Allen, C., Anderson, D., Ansari, A., Bajt, S., Bastien, R.K., Bassim, N., Borg, J., Brenker, F.E., Bridges, J., Brownlee, D.E., Burchell, M., Burghammer, M., Butterworth, A.L., Changela, H., Cloetens, P., Davis, A.M., Doll, R., Floss, C., Frank, D.R., Gainsforth, Z., Grün, E., Heck, P.R., Hillier, J.K., Hoppe, P., Hudson, B., Huth, J., Hvide, B., Kearsley, A., King, A.J., Lai, B., Leitner, J., Lemelle, L., Leroux, H., Leonard, A., Lettieri, R., Marchant, W., Nittler, L.R., Ogliore, R., Ong, W.J., Postberg, F., Price, M.C., Sandford, S.A., Tresseras, J.-A.S., Schmitz, S., Schoonjans, T., Silversmit, G., Simionovici, A.S., Solé, V.A., Srama, R., Stadermann, F.J., Stephan, T., Sterken, V.J., Stodolna, J., Stroud, R.M., Sutton, S., Trieloff, M., Tsou, P., Tsuchiyama, A., Tyliszczak, T., Vekemans, B., Vincze, L., Von Korff, J., Westphal, A.J., Wordsworth, N., Zevin, D., Zolensky, M.E., >30000 Stardust@home dusters, 2014a. Stardust interstellar preliminary examination III: infrared spectroscopic analysis of interstellar dust candidates. Meteorit. Planet. Sci. 49, 1548–1561.

Bechtel, H.A., Flynn, G.J., Allen, C., Anderson, D., Ansari, A., Bajt, S., Bastien, R.K., Bassim, N., Borg, J., Brenker, F.E., Bridges, J., Brownlee, D.E., Burchell, M., Burghammer, M., Butterworth, A.L., Changela, H., Cloetens, P., Davis, A.M., Doll, R., Floss, C., Frank, D.R., Gainsforth, Z., Grün, E., Heck, P.R., Hillier, J.K., Hoppe, P., Hudson, B., Huth, J., Hvide, B., Kearsley, A., King, A.J., Lai, B., Leitner, J., Lemelle, L., Leroux, H., Leonard, A., Lettieri, R., Marchant, W., Nittler, L.R., Ogliore, R., Ong, W.J., Postberg, F., Price, M.C., Sandford, S.A., Tresseras, J.-A.S., Schmitz, S., Schoonjans, T., Silversmit, G., Simionovici, A.S., Solé, V.A., Srama, R., Stadermann, F.J., Stephan, T., Sterken, V.J., Stodolna, J., Stroud, R.M., Sutton, S., Trieloff, M., Tsou, P., Tsuchiyama, A., Tyliszczak, T., Vekemans, B., Vincze, L., Von Korff, J., Westphal, A.J., Wordsworth, N., Zevin, D., Zolensky, M.E., dusters, S.h., 2014b. Stardust interstellar preliminary examination III: infrared spectroscopic analysis of interstellar dust candidates. Meteorit. Planet. Sci. 49, 1548–1561.

Bei, M., Borland, M., Cai, Y., Elleaume, P., Gerig, R., Harkay, K., Emery, L., Hutton, A., Hettel, R., Nagaoka, R., Robin, D., Steier, C., 2010. The potential of an ultimate storage ring for future light sources. nuclear instruments and methods in physics research section A: accelerators spectrometers. Detect. Assoc. Equip. 622, 518–535.

Beister, M., Kolditz, D., Kalender, W.A., 2012. Iterative reconstruction methods in X-ray CT. Phys. Med. 28, 94–108.

Beitz, E., Blum, J., Mathieu, R., Pack, A., Hezel, D.C., 2013a. Experimental investigation of the nebular formation of chondrule rims and the formation of chondite parent bodies. Geochim. Cosmoch. Acta 116, 41–51.

Beitz, E., Güttler, C., Nakamura, A.M., Tsuchiyama, A., Blum, J., 2013b. Experiments on the consolidation of chondrites and the formation of dense rims around chondrules. Icarus 225, 558–569.

Benedix, G.K., Ketcham, R.A., Wilson, L., McCoy, T.J., Bogard, D.D., Garrison, D.H., Herzog, G.F., Xue, S., Klein, J., Middleton, R., 2008. The formation and chronology of the PAT 91501 impact-melt L chondrite with vesicle-metal-sulfide assemblages. Geochim. Cosmoch. Acta 72, 2417–2428.

Berger, M.J., Hubbell, J.H., Seltzer, S.M., Chang, J., Coursey, J.S., Sukumar, R., Zucker, D.S., Olsen, K., 2010. XCOM: Photon Cross Section Database (version 1.5). National Institute of Standards and Technology, Online http://physics.nist.gov/xcomw.

Bertrand, L., Schöeder, S., Anglos, D., Breese, M.B.H., Janssens, K., Moini, M., Simon, A., 2015. Mitigation strategies for radiation damage in the analysis of ancient materials. TrAC Trends Anal. Chem. 66, 128–145.

Bleuet, P., Gergaud, P., Lemelle, L., Bleuet, P., Tucoulou, R., Cloetens, P., Susini, J., Delette, G., Simionovici, A., 2010. 3D chemical imaging based on a third-generation synchrotron source. TrAC Trends Anal. Chem. 29, 518–527.

Blumenfeld, E.J., Evans, C.A., Oshel, E.R., Liddle, D.A., Beaulieu, K., Zeigler, R., Hanna, R.D., Ketcham, R.A., 2015. Comprehensive non-destructive conservation documentation of lunar samples using high-resolution 3D reconstructions and X-ray CT data. In: Lunar and Planetary Science Conference XLVI, Houston, TX, #2740(abstr.).

Boone, M.N., Garrevoet, J., Tack, P., Scharf, O., Cormode, D.P., Van Loo, D., Pauwels, E., Dierick, M., Vincze, L., Van Hoorebeke, L., 2014. High spectral and spatial resolution X-ray transmission radiography and tomography using a color X-ray camera. Nucl. Instrum. Methods Phys. Res. Sect. A: Accel. Spectrom. Detect. Assoc. Equip. 735, 644–648.

Breiman, L., 2001. Random forests. Mach. Learn. 45, 5–32.

Broennimann, C., Eikenberry, E.F., Henrich, B., Horisberger, R., Huelsen, G., Pohl, E., Schmitt, B., Schulze-Briese, C., Suzuki, M., Tomizaki, T., Toyokawa, H., Wagner, A., 2006. The PILATUS 1M detector. J. Synchrotron Radiat. 13, 120–130.

Brownlow, L., Mayo, S., Miller, P.R., Sheffield-Parker, J., 2006. Towards 50-nanometre resolution with an SEM-hosted X-ray microscope. Microsc. Anal. 20, 13–15.

Buzug, T.M., 2008. Computed Tomography: From Photon Statistics to Modern Cone-Beam CT. Springer-Verlag, Berlin Heidelberg.

Chen, G.-H., Tang, J., Leng, S., 2008. Prior image constrained compressed sensing (PICCS) A method to accurately reconstruct dynamic CT images from highly undersampled projection data sets. Med. Phys. 35, 660–663.

Cloetens, P., Ludwig, W., Boller, E., Peyrin, F., Chlenker, M., Baruchel, J., 2002. 3D Imaging using coherent synchrotron radiation. Image Anal. Stereol. 21, S75–S85.

Cnudde, V., Boone, M.N., 2013. High-resolution X-ray computed tomography in geosciences: a review of the current technology and applications. Earth Sci. Rev. 123, 1–17.

Connolly, H.C., Huss, G.R., Wasserburg, G.J., 2001. On the formation of Fe-Ni metal in Renazzo-like carbonaceous chondrites. Geochim. Cosmoch. Acta 65, 4567–4588.

Consolmagno, G., Britt, D., Macke, R., 2008. The significance of meteorite density and porosity. Chemie der Erde/Geochemistry 68, 1–29.

Cuzzi, J.N., 2004. Blowing in the wind: III Accretion of dust rims by chondrule-sized particles in a turbulent protoplanetary nebula. Icarus 168, 484–497.

De Man, B., Nuyts, J., Dupont, P., Marchal, G., Suetens, P., 1999. Metal streak artifacts in X-ray computed tomography: a simulation study. IEEE Trans. Nucl. Sci. 46, 691–696.

De Witte, Y., Vlassenbroeck, J., Van Hoorebeke, L., 2010. A multiresolution approach to iterative reconstruction algorithms in X-ray computed tomography. IEEE Trans. Image Process. 19, 2419–2427.

Deng, H., Fitts, J.P., Peters, C.A., 2016. Quantifying fracture geometry with X-ray tomography: technique of iterative local thresholding (TILT) for 3D image segmentation. Comput. Geosci. 20, 231–244.

Dodd Jr., R.T., 1965. Preferred orientation of chondrules in chondrites. Icarus 4, 308–316.

Eastwood, D.S., Bradley, R.S., Tariq, F., Cooper, S.J., Taiwo, O.O., Gelb, J., Merkle, A., Brett, D.J.L., Brandon, N.P., Withers, P.J., Lee, P.D., Shearing, P.R., 2014. The application of phase contrast X-ray techniques for imaging Li-ion battery electrodes. Nucl. Instrum. Methods Phys. Res. Sect. B 324, 118–123.

Ebel, D.S., Rivers, M.L., 2007. Meteorite 3-D synchrotron microtomography: methods and applications. Meteorit. Planet. Sci. 42, 1627–1646.

Ebel, D.S., Weisberg, M.K., Hertz, J., Campbell, A.J., 2008. Shape, metal abundance, chemistry, and origin of chondrules in the Renazzo (CR) chondrite. Meteorit. Planet. Sci. 43, 1725–1740.

Ebel, D.S., Greenberg, M., Rivers, M.L., Newville, M., 2009. Three-dimensional textural and compositional analysis of particle tracks and fragmentation history in aerogel. Meteorit. Planet. Sci. 44, 1445–1463.

Ebihara, M., Shirai, N., Sekimoto, S., Nakamura, T., Tsuchiyama, A., Matsuno, J., Matsumoto, T., Tanaka, M., Abe, M., Fujimura, A., Ishibashi, Y., Karouji, Y., Mukai, T., Okada, T., Uesugi, M., Yada, T., 2015. Chemical and mineralogical compositions of two grains recovered from asteroid Itokawa. Meteorit. Planet. Sci. 50, 243–254.

Edey, D.R., McCausland, P.J.A., Holdsworth, D.W., Flemming, R.L., 2013. Extended dynamic range micro-computed tomography of meteorites using a biomedical scanner. In: Lunar and Planetary Science Conference XLIV, The Woodlands, TX, #2693(abstr.).

Egan, C.K., Jacques, S.D.M., Wilson, M.D., Veale, M.C., Seller, P., Beale, A.M., Pattrick, R.A.D., Withers, P.J., Cernik, R.J., 2015. 3D chemical imaging in the laboratory by hyperspectral X-ray computed tomography. Sci. Rep. 5, 15979.

Eggl, E., Schleede, S., Bech, M., Achterhold, K., Loewen, R., Ruth, R.D., Pfeiffer, F., 2015. X-ray phase-contrast tomography with a compact laser-driven synchrotron source. Proc. Natl. Acad. Sci. 112, 5567–5572.

Elangovan, P., Hezel, D.C., Howard, L., Armstrong, R., Abel, R.L., 2012. PhaseQuant: a tool for quantifying tomographic data sets of geological specimens. Comput. Geosci. 48, 323–329.

Espes, E., Andersson, T., Björnsson, F., Gratorp, C., Hansson, B.A.M., Hemberg, O., Johansson, G., Kronstedt, J., Otendal, M., Tuohimaa, T., Takman, P., 2014. Liquid-metal-jet x-ray tube technology and tomography applications. In: Proc. SPIE 9212, Developments in X-ray Tomography IX, San Diego, CA, #92120J(abstr.).

Fang, X., Klaus, M., 2007. Real-time 3D computed tomographic reconstruction using commodity graphics hardware. Phys. Med. Biol. 52, 3405.

Feser, M., Holzner, C., Lauridsen, E.M., 2015. Laboratory x-ray micro-tomography system with crystallographic grain orientation mapping capabilities. Google Patents.

Flynn, G.J., Rivers, M.L., Sutton, S.R., Eng, P., Klock, W., 2000. X-ray computed microtomography (CMT): A non-invasive screening tool for characterization of returned rock cores from mars and other solar system bodies. In: Lunar and Planetary Science XXXI, Houston, TX, #1893(abstr.).

Friedrich, J.M., Rivers, M.L., 2013. Three-dimensional imaging of ordinary chondrite microporosity at 2.6 μm resolution. Geochim. Cosmoch. Acta 116, 63–70.

Friedrich, J.M., Macke, R.J., Wignarajah, D.P., Rivers, M.L., Britt, D.T., Ebel, D.S., 2008a. Pore size distribution in an uncompacted equilibrated ordinary chondrite. Planet. Space Sci. 56, 895–900.

Friedrich, J.M., Wignarajah, D.P., Chaudhary, S., Rivers, M.L., Nehru, C.E., Ebel, D.S., 2008b. Three-dimensional petrography of metal phases in equilibrated L chondrites-Effects of shock loading and dynamic compaction. Earth Planet. Sci. Lett. 275, 172–180.

Friedrich, J.M., Ruzicka, A., Rivers, M.L., Ebel, D.S., Thostenson, J.O., Rudolph, R.A., 2013. Metal veins in the Kernouve (H6 S1) chondrite: evidence for pre- or syn-metamorphic shear deformation. Geochim. Cosmoch. Acta 116, 71–83.

Friedrich, J.M., Rubin, A.E., Beard, S.P., Swindle, T.D., Isachsen, C.E., Rivers, M.L., Macke, R.J., 2014a. Ancient porosity preserved in ordinary chondrites: examining shock and compaction on young asteroids. Meteorit. Planet. Sci. 49, 1214–1231.

Friedrich, J.M., Weisberg, M.K., Rivers, M.L., 2014b. Multiple impact events recorded in the NWA 7298 H chondrite breccia and the dynamical evolution of an ordinary chondrite asteroid. Earth Planet. Sci. Lett. 394, 13–19.

Friedrich, J.M., Glavin, D.P., Rivers, M.L., Dworkin, J.P., 2016. Effect of a synchrotron X-ray microtomography imaging experiment on the amino acid content of a CM chondrite. Meteorit. Planet. Sci. 51, 429–437.

Friedrich, J.M., 2008. Quantitative methods for three-dimensional comparison and petrographic description of chondrites. Comput. Geosci. 34, 1926–1935.

Friedrich, J.M., 2014. A classroom-Based distributed workflow initiative for the early involvement of undergraduate students in scientific research. J. Sci. Educ. Technol. 23, 59–66.

Fusseis, F., Xiao, X., Schrank, C., De Carlo, F., 2014. A brief guide to synchrotron radiation-based microtomography in (structural) geology and rock mechanics. J. Struct. Geol. 65, 1–16.

Gattacceca, J., Rochette, P., Denise, M., Consolmagno, G., Folco, L., 2005. An impact origin for the foliation of chondrites [rapid communication]. Earth Planet. Sci. Lett. 234, 351–368.

Gattacceca, J., Suavet, C., Rochette, P., Weiss, B.P., Winklhofer, M., Uehara, M., Friedrich, J.M., 2014. Metal phases in ordinary chondrites: magnetic hysteresis properties and implications for thermal history. Meteorit. Planet. Sci. 49, 652–676.

Gnos, E., Hofmann, B., Franchi, I.A., Al-Kathiri, A., Huser, M., Moser, L., 2002. Sayh al Uhaymir 094: a new martian meteorite from the Oman desert. Meteorit. Planet. Sci. 37, 835–854.

Grady, L., 2006. Random walks for image segmentation. IEEE Trans. Pattern Anal. Mach. Intell. 28, 1768–1783.

Grant, J.A., Davis, J.R., Wells, P., Morgan, M.J., 1994. X-ray diffraction tomography at the australian national beamline facility. Opt. Eng. 33, 2803–2807.

Griffin, L.D., Elangovan, P., Mundell, A., Hezel, D.C., 2012. Improved segmentation of meteorite micro-CT images using local histograms. Comput. Geosci. 39, 129–134.

Hanna, R.D., Ketcham, R.A., 2015. 3D measurement of fine-grained rims in CM murchison using XCT. In: Met. Soc. Meeting LXXVIII, Berkeley, California, #5350(abstr.).

Hanna, R.D., Ketcham, R.A., Hamilton, V.E., 2012. Inclusion foliation in Murchison as revealed by high resolution X-ray CT. In: Lunar Planet. Sci. XLIII, Lunar Planet. Inst., Houston, #1242(abstr.).

Hanna, R.D., Ketcham, R.A., Zolensky, M., Behr, W., 2015. Impact-induced brittle deformation, porosity loss, and aqueous alteration in the Murchison CM chondrite. Geochim. Cosmoch. Acta 171, 256–282.

Hansen, C.D., Johnson, C.R., 2005. The Visualization Handbook. Academic Press, Burlington, MA.

Hemberg, O., Otendal, M., Hertz, H.M., 2003. Liquid-metal-jet anode electron-impact x-ray source. Appl. Phys. Lett. 83, 1483–1485.

Herbig, M., King, A., Reischig, P., Proudhon, H., Lauridsen, E.M., Marrow, J., Buffière, J.-Y., Ludwig, W., 2011. 3-D growth of a short fatigue crack within a polycrystalline microstructure studied using combined diffraction and phase-contrast X-ray tomography. Acta Mater. 59, 590–601.

Herman, G.T., 1979. Correction for beam hardening in computed tomography. Phys. Med. Biol. 24, 81–106.

Hertz, J., Ebel, D.S., Weisberg, M.K., 2003. Tomographic study of shapes and metal abundances of Renazzo chondrules. In: Lunar and Planetary Science Conference XXXIV, Houston, TX, #1959(abstr.).

Hezel, D.C., Elangovan, P., Viehmann, S., Howard, L., Abel, R.L., Armstrong, R., 2013a. Visualisation and quantification of CV chondrite petrography using micro-tomography. Geochim. Cosmoch. Acta 116, 33–40.

Hezel, D.C., Friedrich, J.M., Uesugi, M., 2013b. Looking inside: 3D structures of meteorites. Geochim. Cosmoch. Acta 116, 1–4.

Hirano, T., Minoru, F., Nagata, T., Taguchi, I., Hamada, H., Usami, K., Hayakawa, K., 1990. Observation of Allende and Antarctic meteorites by monochromatic X-ray CT based on synchrotron radiation. In: Fourteenth Symposium on Antarctic Meteorites, Tokyo, #270-281(abstr.).

Hounsfield, G.N., 1973. Computerized transverse axial scanning (tomography). Br. J. Radiol. 46, 1016–1022.

Hounsfield G.N., 1976. Apparatus for examining a body by radiation such as X or gamma radiation. British Patent No 1.283.915, London.

Hsieh, J., 2009. Computed Tomography: Principles, Design, Artifacts, and Recent Advances, Second ed. SPIE John Wiley & Sons Inc., Bellingham, Washington Hooken, New Jersey.

Ikeda, S., Nakano, T., Tsuchiyama, A., Uesugi, K., Suzuki, Y., Nakamura, K., Nakashima, Y., Yoshida, H., 2004. Nondestructive three-dimensional element-concentration mapping of a Cs-doped partially molten granite by X-ray computed tomography using synchrotron radiation. Am. Mineral. 89, 1304–1313.

Jaffray, D.A., Siewerdsen, J.H., Drake, D.G., 1999. Performance of a volumetric CT scanner based upon a flat-panel imager. In: Proc. SPIE 3659, Medical Imaging 1999: Physics of Medical Imaging, San Diego, CA, #204-214(abstr.).

Jenniskens, P., Rubin, A.E., Yin, Q.-Z., Sears, D.W.G., Sandford, S.A., Zolensky, M.E., Krot, A.N., Blair, L., Kane, D., Utas, J., Verish, R., Friedrich, J.M., Wimpenny, J., Eppich, G.R., Ziegler, K., Verosub, K.L., Rowland, D.J., Albers, J., Gural, P.S., Grigsby, B., Fries, M.D., Matson, R., Johnston, M., Silber, E., Brown, P., Yamakawa, A., Sanborn, M.E., Laubenstein, M., Welten, K.C., Nishiizumi, K., Meier, M.M.M., Busemann, H., Clay, P., Caffee, M.W., Schmitt-Kopplin, P., Hertkorn, N., Glavin, D.P., Callahan, M.P., Dworkin, J.P., Wu, Q., Zare, R.N., Grady, M., Verchovsky, S., Emel'Yanenko, V., Naroenkov, S., Clark, D.L., Girten, B., Worden, P.S., 2014. Fall, recovery, and characterization of the Novato L6 chondrite breccia. Meteorit. Planet. Sci. 49, 1388–1425.

Jerram, D.A., Higgins, M.D., 2007. 3D analysis of rock textures: quantifying igneous microstructures. Elements 3, 239–245.

Johnson, G., King, A., Honnicke, M.G., Marrow, J., Ludwig, W., 2008. X-ray diffraction contrast tomography: a novel technique for three-dimensional grain mapping of polycrystals II. The combined case. J. Appl. Crystallogr. 41, 310–318.

Ketcham, R.A., Carlson, W.D., 2001. Acquisition, optimization and interpretation of X-ray computed tomographic imagery; Applications to the geosciences. Comput. Geosci. 27, 381–400.

Ketcham, R.A., Hanna, R.D., 2014. Beam hardening correction for X-ray computed tomography of heterogeneous natural materials. Comput. Geosci. 67, 49–61.

Ketcham, R.A., Hildebrandt, J., 2014. Characterizing, measuring, and utilizing the resolution of CT imagery for improved quantification of fine-scale features. Nucl. Instrum. Methods Phys. Res., Sect. B 324, 80–87.

Ketcham, R.A., Koeberl, C., 2013. New textural evidence on the origin of carbonado diamond: an example of 3-D petrography using X-ray computed tomography. Geosphere 9, 1336–1347.

Ketcham, R.A., 2005a. Computational methods for quantitative analysis of three-dimensional features in geological specimens. Geosphere 1, 32–41.

Ketcham, R.A., 2005b. Three-dimensional grain fabric measurements using high-resolution X-ray computed tomography. J. Struct. Geol. 27, 1217–1228.

Ketcham, R.A., 2006a. Accurate three-dimensional measurements of features in geological materials from X-ray computed tomography data. In: Desrues, J., Viggiani, G., Bésuelle, P. (Eds.), Advances in X-ray Tomography for Geomaterials. ISTE, London, pp. 143–148.

Ketcham, R.A., 2006b. New algorithms for ring artifact removal. In: Proc. SPIE 6318, Developments in X-Ray Tomography V, San Diego, CA.

King, A., Reischig, P., Adrien, J., Ludwig, W., 2013. First laboratory X-ray diffraction contrast tomography for grain mapping of polycrystals. J. Appl. Crystallogr. 46, 1734–1740.

King, A., Reischig, P., Adrien, J., Peetermans, S., Ludwig, W., 2014. Polychromatic diffraction contrast tomography. Mater. Charact. 97, 1–10.

Kondo, M., Tsuchiyama, A., Hirai, H., Koishikawa, A., 1997. High resolution X-ray computed tomographic (CT) images of chondrites and a chondrule. Antarct. Meteor. Res. 10, 437–447.

Krumm, M., Kasperl, S., Franz, M., 2008. Reducing non-linear artifacts of multi-material objects in industrial 3D computed tomography. NDT & E Int. 41, 242–251.

Krzesińska, A., Gattacceca, J., Friedrich, J.M., Rochette, P., 2015. Impact-related noncoaxial deformation in the Pułtusk H chondrite inferred from petrofabric analysis. Meteorit. Planet. Sci. 50, 401–417.

Krzesińska, A., 2011. High resolution X-ray tomography as a tool for analysis of internal textures in meteorites. Meteorites 1, 3–12.

Kuebler, K.E., McSween Jr., H.Y., Carlson, W.D., Hirsch, D., 1999. Sizes and masses of chondrules and metal-troilite grains in ordinary chondrites: possible implications for nebular sorting. Icarus 141, 96–106.

Kyle, J.R., Ketcham, R.A., 2015. Application of high resolution X-ray computed tomography to mineral deposit origin, evaluation, and processing. Ore Geol. Rev. 65 (Part 4), 821–839.

Kyriakou, Y., Meyer, E., Prell, D., Kachelrieß, M., 2010. Empirical beam hardening correction (EBHC) for CT. Med. Phys. 37, 5179–5187.

LaRoque, S.J., Sidky, E.Y., Pan, X., 2008. Accurate image reconstruction from few-view and limited-angle data in diffraction tomography. J. Opt. Soc. Am. A Opt. Image Sci. Vis. 25, 1772–1782.

Larsson, D.H., Takman, P.A.C., Lundström, U., Burvall, A., Hertz, H.M., 2011. A 24 keV liquid-metal-jet x-ray source for biomedical applications. Rev. Sci. Instrum. 82, 123701.

Leitner, C., Hofmann, P., Marschallinger, R., 2014. 3D-modeling of deformed halite hopper crystals by Object Based Image Analysis. Comput. Geosci. 73, 61–70.

Lemelle, L., Simionovici, A., Truche, R., Rau, C., Chukalina, M., Gillet, P., 2004. A new nondestructive X-ray method for the determination of the 3D mineralogy at the micrometer scale. Am. Mineral., 547, http://dx.doi.org/10.2138/am-2004-0409.

Lindgren, P., Hanna, R.D., Dobson, K.J., Tomkinson, T., Lee, M.R., 2015. The paradox between low shock-stage and evidence for compaction in CM carbonaceous chondrites explained by multiple low-intensity impacts. Geochim. Cosmoch. Acta 148, 159–178.

Liu, J., Regenauer-Lieb, K., Hines, C., Liu, K., Gaede, O., Squelch, A., 2009. Improved estimates of percolation and anisotropic permeability from 3D X-ray microtomography using stochastic analyses and visualization. Geochem. Geophys. Geosyst. 10, Q05010.

Ludwig, W., Lauridsen, E.M., Schmidt, S., Poulsen, H.F., Baruchel, J., 2007. High-resolution three-dimensional mapping of individual grains in polycrystals by topotomography. J. Appl. Crystallogr. 40, 905–911.

Macke, R.J., Consolmagno, G.J., Britt, D.T., 2011. Density, porosity, and magnetic susceptibility of carbonaceous chondrites. Meteorit. Planet. Sci. 46, 1842–1862.

Maire, E., Withers, P.J., 2014. Quantitative X-ray tomography. Int. Mater. Rev. 59, 1–43.

Martin, P.M., Mills, A.A., 1980. Preferred chondrule orientations in meteorites. Earth Planet. Sci. Lett. 51, 18–25.

Masuda, A., Taguchi, I., Tanaka, K., 1986. Non-destructive analysis of meteorites by using a high-energy X-ray CT scanner. In: Symposium on Antarctic Meteorites XI, Tokyo, #148-149(abstr.).

Matsumoto, T., Tsuchiyama, A., Nakamura-Messenger, K., Nakano, T., Uesugi, K., Takeuchi, A., Zolensky, M.E., 2013. Three-dimensional observation and morphological analysis of organic nanoglobules in a carbonaceous chondrite using X-ray micro-tomography. Geochim. Cosmoch. Acta 116, 84–95.

Mayo, S.C., Miller, P.R., Sheffield-Parker, J., Gureyev, T.E., Wilkins, S.W., 2005. Attainment of <60 nm resolution in phase-contrast X-ray microscopy using an add-on to an SEM. In: Proc. 8th Int. Conf. X-ray Microscopy, Himeji, Japan.

Mayo, S., Miller, P., Gao, D., Sheffield-Parker, J., 2007. Software image alignment for X-ray microtomography with submicrometre resolution using a SEM-based X-ray microscope. J. Microsc. 228, 257–263.

Mayo, S., Josh, M., Nesterets, Y., Esteban, L., Pervukhina, M., Clennell, M.B., Maksimenko, A., Hall, C., 2015. Quantitative micro-porosity characterization using synchrotron micro-CT and xenon K-edge subtraction in sandstones, carbonates, shales and coal. Fuel 154, 167–173.

McDonald, S.A., Reischig, P., Holzner, C., Lauridsen, E.M., Withers, P.J., Merkle, A.P., Feser, M., 2015. Non-destructive mapping of grain orientations in 3D by laboratory X-ray microscopy. Sci. Rep. 5, 14665.

Meng, L.J., Li, N., La Riviere, P.J., 2011. X-ray fluorescence emission tomography (XFET) with novel imaging geometries –A Monte Carlo study. IEEE Trans. Nucl. Sci. 58, 3359–3369.

Mittlefehldt, D.W., Lindstrom, M.M., 2001. Petrology and geochemistry of Patuxent Range 91501, a clast-poor impact melt from the L-chondrite parent body and Lewis Cliff 88663, an L7 chondrite. Meteorit. Planet. Sci. 36, 439–457.

Moini, M., Rollman, C.M., Bertrand, L., 2014. Assessing the impact of synchrotron X-ray irradiation on proteinaceous specimens at macro and molecular levels. Anal. Chem. 86, 9417–9422.

Mokso, R., Marone, F., Haberthür, D., Schittny, J.C., Mikuljan, G., Isenegger, A., Stampanoni, M., 2011. Following dynamic processes by X-ray tomographic microscopy with sub-second temporal resolution. AIP Conf. Proc. 1365, 38–41.

Myers, G.R., Kingston, A.M., Varslot, T.K., Turner, M.L., Sheppard, A.P., 2011. Dynamic tomography with a priori information. Appl. Opt. 50, 3685–3690.

Nakamura, T., Noguchi, T., Tsuchiyama, A., Ushikubo, T., Kita, N.T., Valley, J.W., Zolensky, M.E., Kakazu, Y., Sakamoto, K., Mashio, E., Uesugi, K., Nakano, T., 2008a. Chondrulelike objects in short-period comet 81P/Wild 2. Science 321, 1664–1667.

Nakamura, T., Tsuchiyama, A., Akaki, T., Uesugi, K., Nakano, T., Takeuchi, A., Suzuki, Y., Noguchi, T., 2008b. Bulk mineralogy and three-dimensional structures of individual Stardust particles deduced from synchrotron X-ray diffraction and microtomography analysis. Meteorit. Planet. Sci. 43, 247–259.

Nakamura, T., Noguchi, T., Tanaka, M., Zolensky, M.E., Kimura, M., Tsuchiyama, A., Nakato, A., Ogami, T., Ishida, H., Uesugi, M., Yada, T., Shirai, K., Fujimura, A., Okazaki, R., Sandford, S.A., Ishibashi, Y., Abe, M., Okada, T., Ueno, M., Mukai, T., Yoshikawa, M., Kawaguchi, J., 2011. Itokawa dust particles: a direct link between S-type asteroids and ordinary chondrites. Science 333, 1113–1116.

Nakano, T., Tsuchiyama, A., Uesugi, K., Uesugi, M., Shinohara, K., 2006. Slice–Softwares for Basic 3-D Analysis. Japan Synchrotron Radiation Research Institute (JASRI), Slice Home Page (web) http://www-bl20. spring8. or.jp/slice/.

Needham, A.W., Abel, R.L., Tomkinson, T., Grady, M.M., 2013. Martian subsurface fluid pathways and 3D mineralogy of the Nakhla meteorite. Geochim. Cosmoch. Acta 116, 96–110.

Nettles, J.W., Lofgren, G.E., Carlson, W.D., McSween, H.Y., 2006. Extent of chondrule melting: evaluation of experimental textures, nominal grain size, and convolution index. Meteorit. Planet. Sci. 41, 1059–1071.

Petrou, M., Garcia Sevilla, P., 2006. Image Processing: Dealing with Texture. Wiley, New York.

Poludniowski, G., Landry, G., DeBlois, F., Evans, P.M., Verhaegen, F., 2009. SpekCalc: a program to calculate photon spectra from tungsten anode X-ray tubes. Phys. Med. Biol. 54, N433.

Popova, O.P., Jenniskens, P., Emel Äôyanenko, V., Kartashova, A., Biryukov, E., Khaibrakhmanov, S., Shuvalov, V., Rybnov, Y., Dudorov, A., Grokhovsky, V.I., Badyukov, D.D., Yin, Q.-Z., Gural, P.S., Albers, J., Granvik, M., Evers, S.G., Kuiper, J., Kharlamov, V., Solovyov, A., Rusakov, Y.S., Korotkiy, S., Serdyuk, I., Korochantsev, A.V., Larionov, M.Y., Glazachev, D., Mayer, A.E., Gisler, G., Gladkovsky, S.V., Wimpenny, J., Sanborn, M.E., Yamakawa, A., Verosub, K.L., Rowland, D.J., Roeske, S., Botto, N.W., Friedrich, J.M., Zolensky, M.E., Le, L., Ross, D., Ziegler, K., Nakamura, T., Ahn, I., Lee, J.I., Zhou, Q., Li, X.-H., Li, Q.-L., Liu, Y., Tang, G.-Q., Hiroi, T., Sears, D., Weinstein, I.A., Vokhmintsev, A.S., Ishchenko, A.V., Schmitt-Kopplin, P., Hertkorn, N., Nagao, K., Haba, M.K., Komatsu, M., Mikouchi, T., 2013. Chelyabinsk airburst, damage assessment, meteorite recovery, and characterization. Science 342, 1069–1073.

Poulsen, H.F., 2004. Three-dimensional X-ray diffraction microscopy. In: Mapping Polycrystals and Their Dynamics. Springer, Berlin.

Rasband, W.S., 1997–2015. ImageJ. U.S. National Institutes of Health, Bethesda, Maryland USA http://imagej.nih.gov/ij/.

Reich, E.S., 2013. Ultimate upgrade for US synchrotron. Nature 501, 148–149.

Remeysen, K., Swennen, R., 2008. Application of microfocus computed tomography in carbonate reservoir characterization: possibilities and limitations. Mar. Petrol. Geol. 25, 486–499.

Rubin, A.E., Swindle, T.D., 2011. Flattened chondrules in the LAP 04581 LL5 chondrite: evidence for an oblique impact into LL3 material and subsequent collisional heating. Meteorit. Planet. Sci. 46, 587–600.

Rubin, A.E., Ulff-Moller, F., Wasson, J.T., Carlson, W.D., 2001. The Portales Valley meteorite breccia: evidence for impact-induced melting and metamorphism of an ordinary chondrite. Geochim. Cosmoch. Acta 65, 323–342.

Russell, S.S., Howard, L., 2013. The texture of a fine-grained calcium-aluminium-rich inclusion (CAI) in three dimensions and implications for early solar system condensation. Geochim. Cosmoch. Acta 116, 52–62.

Ruzicka, A., Brown, R., Friedrich, J., Hutson, M., Hugo, R., Rivers, M., 2015. Shock-induced mobilization of metal and sulfide in planetesimals: evidence from the Buck Mountains 005 (L6 S4) dike-bearing chondrite. Am. Mineral. 100, 2725–2738.

Sakdinawat, A., Attwood, D., 2010. Nanoscale X-ray imaging. Nat. Photon. 4, 840–848.

Sasso, M.R., Macke, R.J., Boesenberg, J.S., Britt, D.T., Rivers, M.L., Ebel, D.S., Friedrich, J.M., 2009. Incompletely compacted equilibrated ordinary chondrites. Meteorit. Planet. Sci. 44, 1743–1753.

Sears, D.W.G., Ninagawa, K., Singhvi, A.K., 2013. Luminescence studies of extraterrestrial materials: insights into their recent radiation and thermal histories and into their metamorphic history. Chemie der Erde – Geochemistry 73, 1–37.

Sears, D., Ebel, D.S., Wallace, S.W., Friedrich, J.M., 2015. X-ray computed tomography and the radiation history of meteorites. In: 78th Annual Meeting of the Meteoritical Society, Berkeley, CA, #5156(abstr.).

Sears, D., Sears, H., Ebel, D.S., Wallace, S.W., Friedrich, J.M., 2016. X-ray computed tomography imaging: a not-so-nondestructive technique. Meteorit. Planet. Sci. 51, 833–838.

Seibert, J.A., 2006. Flat-panel detectors: how much better are they? Pediatr. Radiol. 36, 173–181.

Sham, T.K., Rivers, M.L., 2002. A brief overview of synchrotron radiation. Rev. Mineral. Geochem. 49, 117–147.

Sidky, E.Y., Kao, C.-M., Pan, X., 2006. Accurate image reconstruction from few-views and limited-angle data in divergent-beam CT. J. X-Ray Sci. Technol. 14, 119–139.

Simionovici, A., Allen, C., Bajt, S., Bastien, R., Bechtel, H., Borg, J., Brenker, F.E., Bridges, J.C., Brownlee, D.E., Cloetens, P., Davis, A.M., Floss, C., Flynn, G.J., Frank, D., Gainsforth, Z., Grun, E., Heck, P.R., Hillier, J., Hoppe, P., Howard, L., Huss, G.R., Huth, J., Kearsley, A.T., King, A.J., Lai, B., Leitner, J., Lemelle, L., Leroux, H., Lettieri, R., Marchant, W., Nittler, L.R., Ogliore, R., Postberg, F., Sandford, S., Sans Tresseras, J.A., Schoonjans, T., Schmitz, S., Silvermit, G., Sole, V.A., Srama, R., Stephan, T., Stodolna, J., Stroud, R.M., Sutton, S.R., Trieloff, M., Tsou, P., Tsuchiyama, A., Tyliczszak, T., Vekemans, B., Vincze, L., Westphal, A.J., Zevin, D., Zolensky, M., 2011. Synchrotron X-ray irradiation of Stardust interstellar candidates: from No to Low damage effects. In: 74th Annual Meteoritical Society Meeting, London, #5517(abstr.).

Sonka, M., Hlavac, V., Boyle, R., 2014. Image Processing, Analysis, and Machine Vision, fourth ed. Cengage Learning, Stamford, CT.

Tait, A.W., Tomkins, A.G., Godel, B.M., Wilson, S.A., Hasalova, P., 2014. Investigation of the H7 ordinary chondrite, Watson 012: Implications for recognition and classification of Type 7 meteorites. Geochim. Cosmoch. Acta 134, 175–196.

Tkachuk, A., Duewer, F., Cui, H., Feser, M., Wang, S., Yun, W., 2007. X-ray computed tomography in Zernike phase contrast mode at 8 keV with 50-nm resolution using Cu rotating anode X-ray source. Zeitschrift für Kristallographie – Cryst. Mater. 222, 650–655.

Tomkinson, T., Lee, M.R., Mark, D.F., Dobson, K.J., Franchi, I.A., 2015. The Northwest Africa (NWA) 5790 meteorite: a mesostasis-rich nakhlite with little or no Martian aqueous alteration. Meteorit. Planet. Sci. 50, 287–304.

Tsuchiyama, A., Kawabata, T., Kondo, M., Uesugi, M., Nakano, T., Suzuki, Y., Yagi, N., Umetani, K., Shirono, S., 2000. Spinning chondrules deduced from their three-dimensional structures by X-ray CT method. In: Lunar and Planetary Science Conference XXXI, Houston, TX, #1566(abstr.).

Tsuchiyama, A., Nakamura, T., Nakano, T., Nakamura, N., 2002. Three-dimensional description of the Kobe meteorite by micro X-ray CT method: possibility of three-dimensional curation of meteorite samples. Geochem. J. 36, 369–390.

Tsuchiyama, A., Uesugi, K., Nakano, T., Ikeda, S., 2005. Quantitative evaluation of attenuation contrast of X-ray computed tomography images using monochromatized beams. Am. Mineral. 90, 132–142.

Tsuchiyama, A., Uesugi, M., Matsushima, T., Michikami, T., Kadono, T., Nakamura, T., Uesugi, K., Nakano, T., Sandford, S.A., Noguchi, R., Matsumoto, T., Matsuno, J., Nagano, T., Imai, Y., Takeuchi, A., Suzuki, Y., Ogami, T., Katagiri, J., Ebihara, M., Ireland, T.R., Kitajima, F., Nagao, K., Naraoka, H., Noguchi, T., Okazaki, R., Yurimoto, H., Zolensky, M.E., Mukai, T., Abe, M., Yada, T., Fujimura, A., Yoshikawa, M., Kawaguchi, J., 2011. Three-dimensional structure of hayabusa samples: origin and evolution of Itokawa regolith. Science 333, 1125–1128.

Tsuchiyama, A., Nakano, T., Uesugi, K., Uesugi, M., Takeuchi, A., Suzuki, Y., Noguchi, R., Matsumoto, T., Matsuno, J., Nagano, T., Imai, Y., Nakamura, T., Ogami, T., Noguchi, T., Abe, M., Yada, T., Fujimura, A., 2013. Analytical dual-energy microtomography: a new method for obtaining three-dimensional mineral phase images and its application to Hayabusa samples. Geochim. Cosmoch. Acta 116, 5–16.

Uesugi, K., Takeuchi, A., Suzuki, Y., 2006. Development of micro-tomography system with Fresnel zone plate optics at SPring-8. In: Proc. SPIE 6318, Developments in X-ray Tomography V, San Diego, CA, #63181F(abstr.).

Uesugi, M., Uesugi, K., Oka, M., 2010. Non-destructive observation of meteorite chips using quantitative analysis of optimized X-ray micro-computed tomography. Earth Planet. Sci. Lett. 299, 359–367.

Uesugi, M., Uesugi, K., Takeuchi, A., Suzuki, Y., Hoshino, M., Tsuchiyama, A., 2013. Three-dimensional observation of carbonaceous chondrites by synchrotron radiation X-ray CT – Quantitative analysis and developments for the future sample return missions. Geochim. Cosmoch. Acta 116, 17–32.

Van Geet, M., Swennen, R., Wevers, M., 2000. Quantitative analysis of reservoir rocks by microfocus X-ray computerised tomography. Sediment. Geol. 132, 25–36.

Van Gompel, G., Van Slambrouck, K., Defrise, M., Batenburg, K.J., de Mey, J., Sijbers, J., Nuyts, J., 2011. Iterative correction of beam hardening artifacts in CT. Med. Phys. 38, S36–S49.

Varslot, T., Kingston, A., Myers, G., Sheppard, A., 2011. High-resolution helical cone-beam micro-CT with theoretically-exact reconstruction from experimental data. Med. Phys. 38, 5459.

Vonlanthen, P., Rausch, J., Ketcham, R.A., Putlitz, B., Baumgartner, L.P., Grobéty, B., 2015. High-resolution 3D analyses of the shape and internal constituents of small volcanic ash particles: the contribution of SEM micro-computed tomography (SEM micro-CT). J. Volcanol. Geotherm. Res. 293, 1–12.

Wildenschild, D., Sheppard, A.P., 2013. X-ray imaging and analysis techniques for quantifying pore-scale structure and processes in subsurface porous medium systems. Adv. Water Resour. 51, 217–246.

Wilkins, S.W., Gureyev, T.E., Gao, D., Pogany, A., Stevenson, A.W., 1996. Phase-contrast imaging using polychromatic hard X-rays. Nature 384, 335–338.

Willmott, P., 2011. An Introduction to Synchrotron Radiation. John Wiley and Sons, Ltd, Singapore.

Withers, P.J., 2007. X-ray nanotomography. Mater. Today 10, 26–34.

Yu, Z., Xiaochuan, P., 2004. Exact image reconstruction on PI-lines from minimum data in helical cone-beam CT. Phys. Med. Biol. 49, 941–959.

Zanda, B., Bourot-Denise, M., Hewins, R.H., Cohen, B.A., Delaney, J.S., Humayun, M., Campbell, A.J., 2002. Accretion textures, iron evaporation, and re-condensation in Renazzo chondrules. In: Lunary and Planetary Science XXXIII, Houston, TX, #1852(abstr.).

Zeigler, R., Almeida, N.V., Sykes, D., Smith, C.L., 2014. X-ray micro-computed tomography of Apollo samples as a curation technique enabling better research. In: 77th Annual Meteoritical Society Meeting, Casablanca, #5436(abstr.).

Zolensky, M., Herrin, J., Mikouchi, T., Ohsumi, K., Friedrich, J., Steele, A., Rumble, D., Fries, M., Sandford, S., Milam, S., Hagiya, K., Takeda, H., Satake, W., Kurihara, T., Colbert, M., Hanna, R., Maisano, J., Ketcham, R., Goodrich, C., Le, L., Robinson, G., Martinez, J., Ross, K., Jenniskens, P., Shaddad, M.H., 2010. Mineralogy and petrography of the Almahata Sitta ureilite. Meteorit. Planet. Sci. 45, 1618–1637.

Zolensky, M., Mikouchi, T., Fries, M., Bodnar, R., Jenniskens, P., Yin Q.-z. Hagiya, K., Ohsumi, K., Komatsu, M., Colbert, M., Hanna, R., Maisano, J., Ketcham, R., Kebukawa, Y., Nakamura, T., Matsuoka, M., Sasaki, S., Tsuchiyama, A., Gounelle, M., Le, L., Martinez, J., Ross, K., Rahman, Z., 2014. Mineralogy and petrography of C asteroid regolith: the sutter's mill CM meteorite. Meteorit. Planet. Sci. 49, 1997–2016.